

Dioxygen Reactivity of Biomimetic Fe(II) Complexes with Noninnocent Catecholate, *o*-Aminophenolate, and *o*-Phenylenediamine Ligands

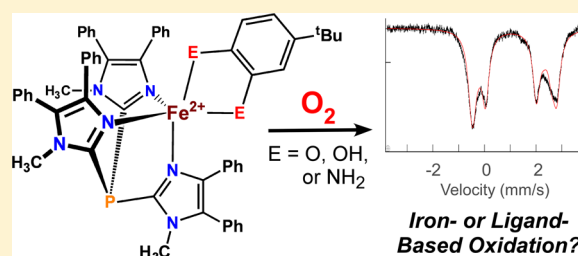
Michael M. Bittner,[†] Sergey V. Lindeman,[†] Codrina V. Popescu,^{*,‡} and Adam T. Fiedler^{*,†}

[†]Department of Chemistry, Marquette University, Milwaukee, Wisconsin 53201, United States

[‡]Department of Chemistry, Ursinus College, Collegeville, Pennsylvania 19426, United States

S Supporting Information

ABSTRACT: This study describes the O₂ reactivity of a series of high-spin mononuclear Fe(II) complexes each containing the facially coordinating tris(4,5-diphenyl-1-methylimidazol-2-yl)phosphine (Ph²TIP) ligand and one of the following bidentate, redox-active ligands: 4-*tert*-butylcatecholate (^tBuCatH[−]), 4,6-di-*tert*-butyl-2-aminophenolate (^tBuAPH[−]), or 4-*tert*-butyl-1,2-phenylenediamine (^tBuPDA). The preparation and X-ray structural characterization of [Fe²⁺(Ph²TIP)(^tBuCatH)]OTf, [3]OTf and [Fe²⁺(Ph²TIP)(^tBuPDA)](OTf)₂, [4](OTf)₂ are described here, whereas [Fe²⁺(Ph²TIP)(^tBuAPH)]OTf, [2]OTf was reported in our previous paper [Bittner et al., *Chem.—Eur. J.* **2013**, *19*, 9686–9698]. These complexes mimic the substrate-bound active sites of nonheme iron dioxxygenases, which catalyze the oxidative ring-cleavage of aromatic substrates like catechols and aminophenols. Each complex is oxidized in the presence of O₂, and the geometric and electronic structures of the resulting complexes were examined with spectroscopic (absorption, EPR, Mössbauer, resonance Raman) and density functional theory (DFT) methods. Complex [3]OTf reacts rapidly with O₂ to yield the ferric-catecholate species [Fe³⁺(Ph²TIP)(^tBuCat)]⁺ (3^{ox}), which undergoes further oxidation to generate an extradiol cleavage product. In contrast, complex [4]²⁺ experiences a two-electron (2e[−]), ligand-based oxidation to give [Fe²⁺(Ph²TIP)(^tBuDIBQ)]²⁺ (4^{ox}), where DIBQ is *o*-diiminobenzoquinone. The reaction of [2]⁺ with O₂ is also a 2e[−] process, yet in this case both the Fe center and ^tBuAP ligand are oxidized; the resulting complex (2^{ox}) is best described as [Fe³⁺(Ph²TIP)(^tBuISQ)]⁺, where ISQ is *o*-iminobenzoquinone. Thus, the oxidized complexes display a remarkable continuum of electronic structures ranging from [Fe³⁺(L^{2−})]⁺ (3^{ox}) to [Fe³⁺(L^{•−})]²⁺ (2^{ox}) to [Fe²⁺(L⁰)]²⁺ (4^{ox}). Notably, the O₂ reaction rates vary by a factor of 10⁵ across the series, following the order [3]⁺ > [2]⁺ > [4]²⁺, even though the complexes have similar structures and Fe^{3+/2+} redox potentials. To account for the kinetic data, we examined the relative abilities of the title complexes to bind O₂ and participate in H-atom transfer reactions. We conclude that the trend in O₂ reactivity can be rationalized by accounting for the role of proton transfer(s) in the overall reaction.



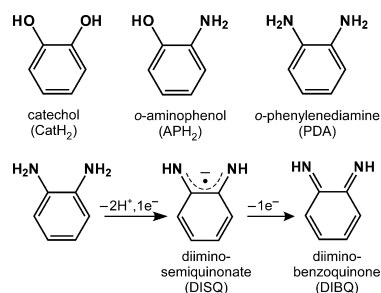
1. INTRODUCTION

Catechols and their nitrogen-containing analogs (*o*-aminophenols and *o*-phenylenediamines; see Scheme 1) are well-established members of the “*o*-phenylene family” of redox noninnocent ligands.^{1–18} One-electron oxidation of these

bidentate ligands provides the corresponding (di)imino-semiquinone radicals, and two-electron oxidation yields the closed-shell (di)imino)benzoquinones. Complexes that combine the noninnocent ligands in Scheme 1 with redox-active metal center(s) often possess ambiguous electronic structures, since multiple assignments of ligand and metal oxidation states are possible. Thus, careful examination with a variety of experimental and computational methods is usually required to obtain accurate electronic-structure descriptions.^{19–23}

While the role of *o*-phenylene ligands in electron-transfer series has been studied extensively, their ability to facilitate *proton-coupled* electron transfers (PCETs) in transition-metal complexes has received less attention. As shown in Scheme 1, the free compounds are able to donate a total of two protons (2H⁺) and two electrons (2e[−]) in various combinations.

Scheme 1. *o*-Phenylene Ligands



Received: December 21, 2013

Published: April 3, 2014

Coordination to a redox-active metal center is expected to perturb the chemical and electronic properties of these ligands, resulting in complexes with rich and unpredictable PCET landscapes. Such complexes may find applications in chemical processes that require multiple proton and electron transfers, including energy-related reactions like water oxidation, hydrogen production, and nitrogen fixation.^{24–29} For instance, an iron complex with *o*-phenylenediamine ligands was recently shown to undergo photochemical H₂-evolution via PCET steps.³⁰ Similarly, Heyduk et al. have found that zirconium(IV) complexes with noninnocent bis(2-phenolato)amide ligands react with O₂ to yield [Zr⁴⁺₂(μ-OH)₂] species—a process that requires donation of 1H⁺ and 2e[−] from each ligand.³¹

Our interest in noninnocent ligands stems from efforts to prepare synthetic mimics of mononuclear nonheme iron dioxygenases. These enzymes carry out the oxidative ring-cleavage of aromatic substrates (catechols, aminophenols, and hydroquinones), and the catalytic cycles are thought to involve formation of a ferrous-(substrate radical) intermediate.^{32–35} Recently, we reported the synthesis of two mononuclear Fe(II) complexes (**1** and **2**)OTf that model the substrate-bound form of aminophenol dioxygenases.^{36,37} The high-spin ferrous centers of **1** and **2**⁺ are bound to the 2-amino-4,6-di-*tert*-butylphenolate (^{*t*}Bu₂APH) “substrate,” and the enzymatic coordination environment is replicated using a facially coordinating N3 supporting ligand: hydrotris(3,5-diphenylpyrazol-1-yl)borate (^{*Ph*}₂Tp) in the case of **1** and tris(4,5-diphenyl-1-methylimidazol-2-yl)phosphine (^{*Ph*}₂TIP) in **2**OTf (see Scheme 2). These complexes were shown to engage in

Fe³⁺–^{*t*}Bu₂ISQ and Fe²⁺–^{*t*}Bu₂IBQ limits,³⁷ where ^{*t*}Bu₂IBQ is iminobenzoquinone with *tert*-butyl substituents at the 4- and 6-positions.

In this Manuscript, we expanded upon our previous studies by preparing monoiron(II) ^{*Ph*}₂TIP-based complexes with ligands derived from catechol and *o*-phenylenediamine. Like the *o*-aminophenolate studies described above, we began with the synthesis and X-ray structural characterization of mononuclear, high-spin Fe(II) complexes, each containing a bidentate ligand capable of both proton and electron transfer. The catecholate complex **[3]OTf** was prepared using 4-*tert*-butylcatechol (^{*t*}BuCatH₂) and the ^{*Ph*}₂TIP supporting ligand (Scheme 2). The *o*-phenylenediamine complex **[4](OTf)₂** has the overall formulation of [Fe(^{*Ph*}₂TIP)(^{*t*}BuPDA)](OTf)₂, where ^{*t*}BuPDA is 4-*tert*-butyl-1,2-phenylenediamine. Each of the three Fe(II) complexes (**[2]**⁺, **[3]**⁺, and **[4]**²⁺) is air-sensitive, and the products of the O₂ reactions have been characterized with spectroscopic (ultraviolet–visible (UV–vis) absorption, electron paramagnetic resonance (EPR), Mössbauer, resonance Raman) and computational (density functional theory (DFT)) methods. These studies revealed that the identity of the ligand controls whether the O₂-driven oxidation is an Fe- or ligand-based process (or a combination of both). In addition, O₂ reaction rates vary by greater than 5 orders of magnitude across the series, despite the fact that the overall structures of the Fe(II) complexes are quite similar. Thus, this unique series of complexes has provided a valuable framework for exploring the relationship between ligand-based PCET chemistry and the O₂ reactivity of Fe complexes. The implications of these results for the O₂ activation mechanisms of the ring-cleaving dioxygenases are also discussed.

Scheme 2

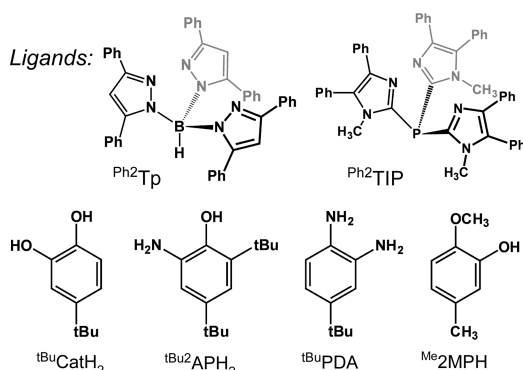
Complexes: **1** = [Fe²⁺(^{*t*}Bu₂APH)(^{*Ph*}₂Tp)]

[2]⁺ = [Fe²⁺(^{*t*}Bu₂APH)(^{*Ph*}₂TIP)]⁺

[3]⁺ = [Fe²⁺(^{*t*}BuCatH)(^{*Ph*}₂TIP)]⁺

[4]²⁺ = [Fe²⁺(^{*t*}BuPDA)(^{*Ph*}₂TIP)]²⁺

[5]⁺ = [Fe²⁺(Me₂MPP)(^{*Ph*}₂TIP)]⁺



ligand-based H-atom transfer (HAT) reactions to yield novel species containing an Fe(II) center coordinated to an iminobenzosemiquinone (^{*t*}Bu₂ISQ) radical, thus providing synthetic precedents for the putative Fe(II)/ISQ intermediate of the enzyme. The Fe(II)/ISQ complexes can be further oxidized by one electron, although it has proven difficult to determine whether this process is ligand- or iron-based. Detailed crystallographic, spectroscopic, and computational analyses suggest that the fully oxidized species have intermediate electronic configurations between the

2. EXPERIMENTAL SECTION

Materials. Reagents and solvents were purchased from commercial sources and were used as received, unless otherwise noted. Air-sensitive materials were synthesized and handled under inert atmosphere using a Vacuum Atmospheres Omni-Lab glovebox. The ^{*Ph*}₂TIP³⁸ and ^{*t*}BuAPH₂³⁹ ligands and the 2,4,6-tri-*tert*-butylphenoxy radical⁴⁰ (TTBP[•]) were prepared according to literature procedures. Synthetic procedures for complexes [Fe(^{*Ph*}₂TIP)(MeCN)₃](OTf)₂,³⁸ **1**,³⁶ and **[2]OTf**³⁷ were published previously by our group.

Physical Methods. Elemental analyses were performed at Midwest Microlab, LLC in Indianapolis, IN. UV–vis absorption spectra were measured with an Agilent 8453 diode array spectrometer equipped with a cryostat from Unisuko Scientific Instruments (Osaka, Japan). Fourier-transform infrared (FTIR) spectra of solid samples were obtained with a Thermo Scientific Nicolet iS5 FTIR spectrometer equipped with the iD3 attenuated total reflectance accessory. ¹H and ¹⁹F NMR spectra were recorded at room temperature with a Varian 400 MHz spectrometer. ¹⁹F NMR spectra were referenced to the benzotrifluoride peak at −63.7 ppm. Mass spectra were collected using an Agilent 6850 gas chromatography–mass spectrometer (GC–MS) with a HP-5 (5% phenylmethylpolysiloxane) column. Cyclic voltammetric (CV) measurements were conducted in the glovebox with an epsilon EC potentiostat (iBAS) at a scan rate of 100 mV/s with 100 mM (NBu₄)PF₆ as the supporting electrolyte. The three-electrode cell contained a Ag/AgCl reference electrode, a platinum auxiliary electrode, and a glassy carbon working electrode. Potentials were referenced to the ferrocene/ferrocenium (Fc^{+/0}) couple, which has E_{1/2} values of +0.52 V in CH₂Cl₂ under these conditions.

EPR experiments were performed using a Bruker ELEXSYS E600 featuring an ER4415DM cavity that resonates at 9.63 GHz, an Oxford Instruments ITC503 temperature controller, and an ESR-900 He flow cryostat. The program EasySpin⁴¹ was used to simulate and fit experimental spectra. Resonance Raman (rR) spectra were measured with excitation from either a Coherent I-305 Ar⁺ laser (488.0 nm) or I-

Table 1. Summary of X-ray Crystallographic Data Collection and Structure Refinement

	[3](OTf)2DCE	[4](OTf)(BPh ₄)-DCE·C ₅ H ₁₂ ^a	[4(MeCN)](OTf) ₂ ·MeCN·Et ₂ O ^b	[5](OTf)·1.5CH ₂ Cl ₂
empirical formula	C ₆₃ H ₆₀ Cl ₄ F ₃ FeN ₆ O ₅ PS	C ₉₀ H ₉₁ BCl ₂ F ₃ FeN ₆ O ₅ PS	C ₆₈ H ₇₁ F ₆ FeN ₁₀ O ₇ PS ₂	C _{58.5} H ₅₁ Cl ₃ F ₃ FeN ₆ O ₅ PS
formula weight	1298.85	1590.34	1388.96	1200.28
crystal system	monoclinic	monoclinic	triclinic	triclinic
space group	<i>P</i> 2 ₁	<i>P</i> 2 ₁ / <i>n</i>	<i>P</i> $\bar{1}$	<i>P</i> $\bar{1}$
<i>a</i> , Å	16.0859(2)	19.6939(4)	15.3998(3)	15.5548(2)
<i>b</i> , Å	21.4779(2)	18.3202(4)	15.6626(3)	17.2278(3)
<i>c</i> , Å	17.8488(2)	22.2057(4)	17.9588(3)	23.4768(4)
α , deg	90	90	88.191(2)	97.790(1)
β , deg	90.1428(9)	92.009(2)	64.934(2)	91.828(1)
γ , deg	90	90	61.081(2)	115.875(2)
<i>V</i> , Å ³	6166.6(1)	8006.8(3)	3351.4(1)	5578.9(2)
<i>Z</i>	4	4	2	4
<i>D</i> _{calc} , g/cm ³	1.399	1.293	1.376	1.429
λ , Å	1.5418	0.7107	0.7107	1.5418
μ , mm ⁻¹	4.642	0.350	0.388	4.654
θ range, deg	6 to 148	6 to 58	6 to 58	6 to 147
reflections collected	60 871	77 363	74 982	71 466
independent	23 500	19 234	16 362	21 895
reflections	[<i>R</i> _{int} = 0.0372]	[<i>R</i> _{int} = 0.0418]	[<i>R</i> _{int} = 0.0363]	[<i>R</i> _{int} = 0.0345]
data/restraints/parameters	23 500/7/1532	19 234/67/1058	16 362/7/898	21 895/129/1607
GOF (on <i>F</i> ²)	1.041	1.051	1.050	1.074
<i>R</i> ₁ / <i>wR</i> ₂ (<i>I</i> > 2 σ (<i>I</i>)) ^b	0.0390/0.1022	0.0962/0.2182	0.0470/0.1170	0.0425/0.1169
<i>R</i> ₁ / <i>wR</i> ₂ (all data) ^b	0.0395/0.1028	0.1280/0.2375	0.0589/0.1253	0.0478/0.1215

^aThe DCE solvate is only partially (80%) populated. ^bThe ethereal solvate is only partially (78%) populated.

302C Kr⁺ laser (647.1 nm) with ~50 mW of power at the sample. The scattered light was collected using a 135° backscattering arrangement, dispersed by an Acton Research triple monochromator equipped with a 1200 grooves/mm grating and detected with a Princeton Instruments Spec X 100BR CCD camera. Spectra were accumulated at 77 K, and rR frequencies were referenced to the 983 cm⁻¹ peak of K₂SO₄.⁴² Low-field (0.04 T) variable temperature (5–200 K) Mössbauer spectra were recorded on a closed-cycle refrigerator spectrometer, model CCR4K, equipped with a 0.04 T permanent magnet, maintaining temperatures between 5 and 300 K. Mössbauer spectra were analyzed using the software WMOSS (Thomas Kent, SeeCo.us, Edina, Minnesota). The samples consisted of solid powders (or crystalline material) suspended in nujol, placed in Delrin 1.00 mL cups, and then frozen in liquid nitrogen. The [4](OTf)₂ sample was prepared from material crystallized from a mixture of 1,2-dichloroethane (DCE) and Et₂O. The air-oxidized sample 4^{ox} was prepared by exposing a solution of [4](OTf)₂ in CH₂Cl₂ to air for 20 h, followed by removal of solvent to give a dark green powder. (In this Manuscript, “ox” designates species generated via reaction of the Fe(II) starting complexes with O₂.) The isomer shifts are quoted at 5 K with respect to iron metal spectra recorded at 298 K.

X-ray diffraction (XRD) data were collected with an Oxford Diffraction SuperNova κ -diffractometer (Agilent Technologies) equipped with dual microfocus Cu/Mo X-ray sources, X-ray mirror optics, Atlas CCD detector, and low-temperature Cryojet device. The data were processed with CrysAlis Pro program package (Agilent Technologies, 2011), followed by an empirical multiscan correction using SCALE3 ABSPACK routine. Structures were solved using SHELXS program and refined with SHELXL program⁴³ within Olex2 crystallographic package.⁴⁴ X-ray crystallographic parameters are provided in Table 1, and experimental details are available in the CIFs.

[Fe(^{Ph₂TIP})(^{tBu}CatH)](OTf), [3]OTf. Equimolar amounts of [Fe(^{Ph₂TIP})(MeCN)₃](OTf)₂ (456 mg, 0.38 mmol) and ^{tBu}CatH₂ (63 mg, 0.38 mmol) were dissolved in tetrahydrofuran (THF) (10 mL), followed by addition of NEt₃ (58 μ L, 0.42 mmol). The dark yellow solution was stirred for 30 min, and the solvent was removed under vacuum. The crude material was taken up in DCE (5 mL) and filtered. Layering of this solution with hexane provided bright yellow crystals suitable for X-ray diffraction. Crystals were washed with hexanes and

dried under vacuum (yield = 83 mg, 20%). μ_{eff} = 4.7 μ_{B} (Evans method). UV–vis [λ_{max} nm (ϵ , M⁻¹ cm⁻¹) in CH₂Cl₂]: 397 (940). IR (neat, cm⁻¹): 3058 (w), 2955 (w), 1603 (w), 1505 (m), 1460 (m), 1443 (m), 1369 (m), 1241 (s), 1154 (s), 1028 (s). ¹H NMR (400 MHz, CD₂Cl₂): δ = -27.52, -10.44, 2.22, 4.51, 5.98, 6.94, 9.53, 10.06, 11.47, 23.88, 29.58, 61.67, 65.98. ¹⁹F NMR (376 MHz, CD₂Cl₂): δ = -80.3 (OTf) ppm. Elemental analysis calcd (%) for C₅₉H₅₂F₃FeN₆O₅PS·2DCE: C, 58.26; H, 4.66; N, 6.47. Found: C, 58.00; H, 4.98; N, 6.46.

[Fe(^{Ph₂TIP})(^{tBu}PDA)](OTf)₂, [4](OTf)₂. Equimolar amounts of [Fe(^{Ph₂TIP})(MeCN)₃](OTf)₂ (304 mg, 0.25 mmol) and ^{tBu}PDA (42 mg, 0.25 mmol) were dissolved in THF (10 mL), and the reaction was stirred for 18 h. Removal of the solvent under vacuum yielded a white solid that was dissolved in DCE (3 mL) and filtered. Vapor diffusion of Et₂O into this solution afforded the product as a colorless solid (yield = 123 mg, 39%) suitable for use in spectroscopic and kinetic studies. The complex does not exhibit absorption features in the visible region. μ_{eff} = 5.48 μ_{B} (Evans method). IR (neat, cm⁻¹): 3306 (w, ν (NH)), 3254 (w, ν (NH)), 3057 (w), 2960 (w), 1572 (w), 1443 (w), 1261 (s), 1147 (m), 1029 (w). ¹H NMR (400 MHz, CD₂Cl₂): δ = -28.8 (1H), 0.62 (9H), 4.98 (6H), 7.00 (3H), 7.32 (3H), 7.68 (6H), 8.53 (6H), 11.81 (1H), 12.89 (9H), 15.33 (6H), 19.01 (2H), 24.33 (2H), 31.36 (1H). ¹⁹F NMR (376 MHz, CD₂Cl₂): δ = -79.3 (OTf) ppm. Elemental analysis revealed that a small amount of DCE solvent (0.5 equiv/Fe) remains after drying. Elemental analysis calcd (%) for C₆₀H₅₅F₆FeN₈O₆PS₂·0.5DCE: C, 56.42; H, 4.42; N, 8.63; F, 8.78. Found: C, 56.56; H, 4.51; N, 8.54; F, 8.32. X-ray quality crystals were obtained by either slow diffusion of Et₂O into a concentrated MeCN solution or pentane layering of a DCE solution containing 1 equiv of NaBPh₄.

[Fe(^{Ph₂TIP})(^{Me}2MP)]OTf, [5]OTf. Equimolar amounts of [Fe(^{Ph₂TIP})(MeCN)₃](OTf)₂ (143 mg, 0.12 mmol) and 2-methoxy-5-methylphenolate (^{Me}2MPH, 16.3 mg, 0.12 mmol) were dissolved in THF (10 mL), followed by addition of NEt₃ (20 μ L, 0.15 mmol). The mixture was stirred for 3 h, and the solvent was removed under vacuum. The crude solid was taken up in CH₂Cl₂ (5 mL) and layered with hexanes. After several days, light green crystals suitable for X-ray crystallography were collected (yield = 101 mg, 80%). UV–vis [λ_{max} nm (ϵ , M⁻¹ cm⁻¹) in CH₂Cl₂]: 390 (1400), 610 (500). IR (neat,

cm⁻¹): 3048 (w), 1597 (w), 1499 (w), 1444 (m), 1396 (w), 1260 (s), 1220 (s), 1146 (s), 1073 (w), 1028 (s), 982 (m), 790 (s), 771 (s). The crystals used for elemental analysis were prepared from a mixture of DCE/hexanes. The results suggest that some DCE solvent (~1 equiv/Fe) remains after drying, consistent with the X-ray structure that found 1.5 equiv of uncoordinated CH₂Cl₂ in the unit cell. Elemental analysis calcd (%) for C₅₇H₄₈F₃FeN₆O₃PS·DCE: C, 60.47; H, 4.47; N, 7.17; Found: C, 59.00; H, 4.63; N, 7.55.

Synthesis of ^tBuPDA with ¹⁵N at 2-Position. Using a published procedure,⁴⁵ acetic anhydride (2.64 g, 25.8 mmol) was added dropwise to a solution of 4-*tert*-butylaniline (3.34 g, 22.4 mmol) in CH₂Cl₂ (30 mL) at 0 °C. A white precipitate formed as the mixture was stirred for 30 min. After addition of 30 mL of hexanes, the solution was filtered to give 4-*tert*-butylacetanilide as a white solid. Without further purification, 680 mg (3.55 mmol) of the product was dissolved in CHCl₃ (15 mL). To this solution, H₂SO₄ (0.3 mL) and ¹⁵N-labeled HNO₃ (1.0 g, 7.04 mmol, Aldrich, 98% ¹⁵N) were added dropwise. The resulting dark orange solution was stirred for 1 h and was then washed successively with H₂O, saturated NaHCO₃, and brine. After drying the organic layer with MgSO₄ the solvent was removed to yield 4-*tert*-butyl-2-nitroacetanilide. The protecting group was then removed by refluxing in EtOH with KOH (143 mg, 2.6 mmol). The mixture was poured into ice–water, yielding a precipitate that was isolated by filtration, washed with cold H₂O, and dried in vacuo. The resulting ¹⁵N-labeled 4-*tert*-butyl-2-nitroaniline (300 mg, 1.54 mmol) was dissolved in MeOH (20 mL), and 5% Pd/C catalyst (90 mg) was added. The mixture was stirred under H₂ (46 psi) for 5 h and filtered through Celite, and the solvent was removed under vacuum to yield a dark purple solid (yield = 201 mg, 79%). ¹H and ¹³C NMR spectra of the product were identical to those obtained with commercially available ^tBuPDA.

Dioxygen Reactivity Studies. Oxygenation studies were performed by injecting anaerobic solutions of the Fe(II) complex into O₂-saturated solutions of CH₂Cl₂ at the desired temperature. Formation of the oxidized species was monitored using UV–vis spectroscopy. The concentration of O₂ in CH₂Cl₂ solutions at various temperatures (*T*) was estimated using the formula: $S = (LP_{O_2})/(TR)$, where *L* is the Ostwald coefficient (0.257 for CH₂Cl₂), *P*_{O₂} is the partial pressure of O₂, and *R* is the gas constant.^{46,47} The determination of *P*_{O₂} accounted for the vapor pressure of CH₂Cl₂ (*P*_{solv}) as a function of *T*: $P_{O_2} = 1 \text{ atm} - P_{solv}$. Following established procedures,^{48–51} the decomposition products of the 3^{ox} + O₂ reaction were isolated by removing the CH₂Cl₂ solvent under vacuum, taking the residue up in MeCN, and treating the solution with ~3 mL of HCl (2 M). After extraction of the aqueous layer with Et₂O, the solvent was removed to give a residue that was analyzed with GC–MS and/or ¹H NMR spectroscopy. The ¹H NMR data was interpreted with the aid of published spectra.⁵²

DFT Computations. DFT calculations were performed using the ORCA 2.9 software package developed by Dr. F. Neese (MPI for Chemical Energy Conversion).⁵³ Calculations involving 4^{ox} employed Becke's three-parameter hybrid functional for exchange along with the Lee–Yang–Parr correlation functional (B3LYP).^{54,55} These calculations utilized Ahlrichs' valence triple- ζ basis set (TZV) and TZV/J auxiliary basis set, in conjunction with polarization functions on all atoms.^{56–58} In the geometry-optimized model, the ^{Ph}2TIP ligand was modified by replacing the Ph-groups at the 5-position of the imidazolyl rings with H-atoms. In addition, the *tert*-butyl substituent of the ^tBuPDA ligand was replaced with an Me group. To avoid spurious transitions, time-dependent DFT (TD-DFT) calculations used a truncated version of the optimized 4^{ox} model with Me groups (instead of Ph groups) at the 4-positions of the imidazolyl rings. TD-DFT calculations^{59–61} calculated absorption energies and intensities for 50 excited states with the Tamm–Dancoff approximation.^{62,63} Isosurface plots of molecular orbitals and electron-density difference maps (EDDMs) were prepared with Laaksonen's gOpenMol program.⁶⁴

Energetic parameters for the binding of O₂ to the Fe(II) complexes were computed using the Perdew–Burke–Ernzerhof (PBE) functional⁶⁵ with 10% Hartree–Fock exchange. These calculations employed modified ^{Ph}2TIP ligands containing three *N*-methylimida-

zole rings attached at the 2-position to a central P atom, and the *tert*-butyl substituents of the bidentate ligand were replaced with Me groups. Geometry optimizations were performed for the Fe(II) precursors, [Fe/O₂] adducts, and O₂ under tight convergence criteria, and the resulting models were used to obtain gas-phase vibrational and thermodynamic data. Solvent effects were calculated using the conductor-like screening model (COSMO)⁶⁶ with a dielectric constant (ϵ) of 9.08 for CH₂Cl₂. The “spin-flip” feature of ORCA was employed to generate [Fe/O₂] wave functions for *S*_{tot} = 2 and 1 states.

3. RESULTS AND ANALYSIS

3.A. Synthesis, X-ray Structures, and Electrochemical Properties. Reaction of [Fe(^{Ph}2TIP)(MeCN)₃](OTf)₂ with ^tBuCatH₂ or ^tBuPDA in THF generated the ^{Ph}2TIP-based complexes [3]OTf and [4](OTf)₂, respectively; the synthesis of [3]⁺ also required 1 equiv of NEt₃.⁶⁷ Yellow crystals of [3]OTf were grown by layering a DCE solution with hexane. Recrystallization of [4](OTf)₂ by slow diffusion of Et₂O into a DCE solution provided colorless and analytically pure material that was used in subsequent reactivity and spectroscopic studies.⁶⁸ Crystals for X-ray diffraction (XRD) analysis were obtained by either (i) slow diffusion of Et₂O into a concentrated MeCN solution of [4](OTf)₂ or (ii) pentane layering of a DCE solution. In the latter case, the resulting crystals diffracted poorly due to extensive disorder of the triflate counteranions. However, by adding 1 equiv of NaBPh₄ to the DCE solution, we were able to grow well-diffracting crystals with an overall composition of [4](OTf)(BPh₄).

As shown in Figure 1, the X-ray structure of [3]OTf features a five-coordinate (5C) Fe(II) complex with bidentate

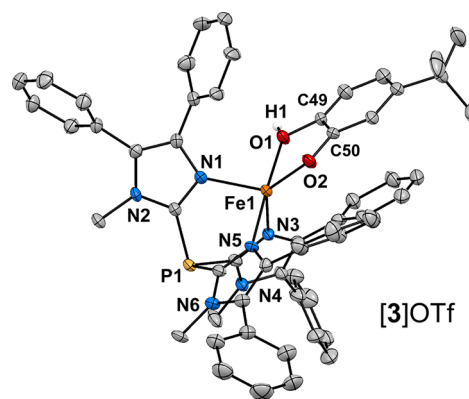


Figure 1. Thermal ellipsoid plot (50% probability) derived from the X-ray structure of [3]OTf·2DCE. Counteranions, noncoordinating solvent molecules, and most hydrogen atoms have been omitted for clarity.

monoanionic catecholates and facially coordinating ^{Ph}2TIP ligands. The [3]OTf unit cell contains two symmetrically independent complexes, and metric parameters for both are provided in Table 2. The Fe(II) coordination geometry is trigonal-bipyramidal for one cation ($\tau = 0.70$)⁶⁹ and distorted square-pyramidal ($\tau = 0.24$) for the other. The crystallographic data provide solid evidence that the catecholates ligand is monoanionic. First, there is a significant difference in the lengths of the O1–C49 and O2–C50 bonds (1.39 and 1.33 Å, respectively). Second, the ^tBuCatH ligand binds asymmetrically with Fe1–O1 bond distances that are ~0.30 Å longer than the corresponding Fe1–O2 bonds. The protonated donor is weakly bound with an Fe1–O1 distance of 2.23 ± 0.01 Å, while the anionic donor exhibits a shorter Fe1–O2 distance of $1.92 \pm$

Table 2. Selected Bond Distances (Å) and Bond Angles (deg) for [3]⁺, [4]²⁺, and [5]⁺ Measured with X-ray Diffraction

	[3]OTf·2DCE ^a		[4](OTf)(BPh ₄)·DCE·C ₅ H ₁₂	[4(MeCN)](OTf) ₂ ·MeCN·Et ₂ O	[5](OTf)·1.5SCH ₂ Cl ₂ ^b
	(A)	(B)			
Fe1–N1	2.118(3)	2.121(3)	2.089(4)	2.174(2)	2.124(2)
Fe1–N3	2.124(3)	2.155(3)	2.115(3)	2.162(2)	2.120(2)
Fe1–N5	2.192(3)	2.192(3)	2.181(3)	2.227(2)	2.142(2)
Fe1–O1/N7	2.226(3)	2.241(3)	2.224(3)	2.237(2)	2.229(2)
Fe1–O2/N8	1.922(3)	1.938(3)	2.131(4)	2.246(2)	1.919(2)
Fe1–N9				2.214(2)	
O1/N7–C49	1.390(5)	1.395(5)	1.445(5)	1.444(2)	1.390(3)
O2/N8–C50	1.323(5)	1.327(5)	1.458(5)	1.454(2)	1.336(3)
N1–Fe1–N3	93.5(1)	94.2(1)	95.3(1)	86.07(6)	94.03(7)
N1–Fe1–N5	91.3(1)	91.9(1)	84.5(1)	91.74(6)	89.20(7)
N3–Fe1–N5	85.4(1)	85.9(1)	91.1(1)	88.90(6)	85.81(7)
N1–Fe1–O1/N7	90.5(1)	102.3(1)	94.7(1)	167.47(6)	90.75(6)
N3–Fe1–O1/N7	90.7(1)	89.6(1)	96.9(1)	99.93(6)	90.21(6)
N5–Fe1–O1/N7	175.7(1)	165.4(1)	172.0(1)	89.59(6)	176.01(6)
N1–Fe1–O2/N8	130.7(1)	114.5(1)	145.3(1)	93.45(6)	124.35(7)
N3–Fe1–O2/N8	133.8(1)	150.3(1)	119.2(1)	172.48(6)	139.32(7)
N5–Fe1–O2/N8	103.7(1)	100.0(1)	92.2(1)	96.87(6)	105.70(7)
O1/N7–Fe1–O2/N8	77.9(1)	77.4(1)	77.8(1)	75.38(6)	77.58(6)
τ-value ^c	0.70	0.24	0.45		0.61

^aThe [3]OTf·2DCE structure contains two symmetry-independent complexes per unit cell. Parameters are provided for both structures. ^bThe [5]OTf·1.5SCH₂Cl₂ structure contains two symmetry-independent complexes per unit cell. Since the structures are nearly identical, parameters are only provided for one complex. ^cSee reference 69 for definition of the τ value.

0.01 Å (Table 2). Such bond distances are generally similar to those observed in the four previously reported Fe(II) complexes with monoanionic catecholate ligands.^{51,70–72} The triflate counteranion forms a hydrogen bond with the hydroxyl group of the ^tBuCatH ligand, consistent with the O1...O3(Tf) distance of ~2.67 Å. The average Fe–N bond distance is 2.150 Å, similar to the corresponding distances measured for the ^tBu₂APH-based complex ([2]⁺) and indicative of a high-spin, pentacoordinate Fe(II) complex.³⁷ Consistent with this fact, the ¹H NMR spectrum displays paramagnetically shifted peaks ranging from 65 to –30 ppm (Supporting Information, Figure S1).

The two X-ray structures of complex [4]²⁺ shown in Figure 2 reflect the different conditions under which the crystals were generated (vide supra). Crystals grown in a DCE/pentane mixture contain a 5C dicationic Fe complex associated with one OTf and one BPh₄ counteranion, in addition to DCE and pentane solvent molecules (Table 1). The coordination environment of the Fe(II) center is intermediate between square-planar and trigonal-bipyramidal (τ = 0.45; Table 2). In contrast, the structure arising from crystals grown in MeCN/Et₂O features a six-coordinate (6C) Fe(II) center bound to a solvent-derived MeCN ligand in addition to ^{Ph}2-TIP and ^tBuPDA (Figure 2). The increase in coordination number lengthens the average Fe–N_{TIP} bond distance from 2.13 Å in [4]²⁺ to 2.19 Å in [4(MeCN)]²⁺. The ^tBuPDA ligand binds symmetrically in the 6C structure (Fe–N_{PDA} distance of 2.24(1) Å), while the Fe1–N7/N8 distances differ by 0.093 Å in the 5C structure. The observed Fe–N bond lengths indicate that the Fe(II) centers are high-spin in both structures. This conclusion is supported by the corresponding ¹H NMR spectrum (Supporting Information, Figure S1) and the measured magnetic moment of 5.48 μ_B in CH₂Cl₂. The neutral charge of the ^tBuPDA ligands is confirmed by the presence of N–C bond lengths of 1.45(1) Å, typical of aryl amines (anilide anions, in contrast, exhibit N–C bond distances of ~1.39 Å). In both structures, the ^tBuPDA

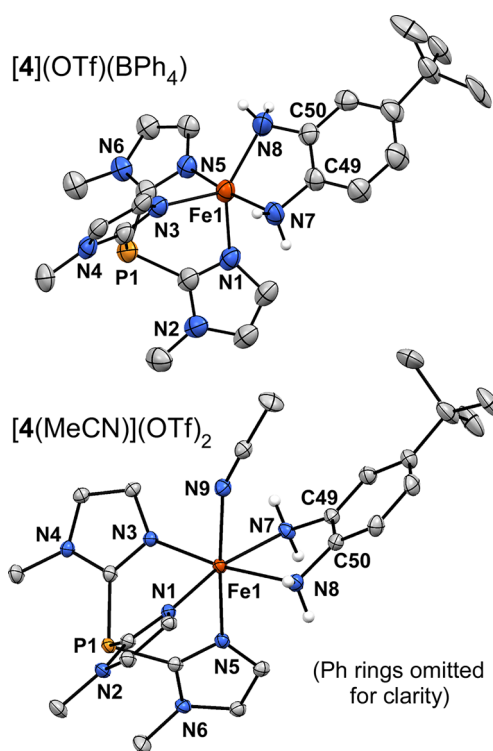


Figure 2. Thermal ellipsoid plots (50% probability) derived from [4](OTf)(BPh₄)·DCE·C₅H₁₂ (top) and [4(MeCN)](OTf)₂·MeCN·Et₂O (bottom). Counteranions, noncoordinating solvent molecules, and most hydrogen atoms have been omitted for clarity. The phenyl rings of the ^{Ph}2-TIP ligands have also been removed to provide a clearer view of the first coordination sphere.

ring tilts out of the plane formed by the N7–Fe1–N8 chelate by ~23°, and each triflate is hydrogen-bonded to an amino group of ^tBuPDA.

As described below, the noninnocent nature of the *o*-phenylene ligands plays an important role in the reactions of the corresponding Fe(II) complexes with O₂. To highlight this phenomenon, we prepared a “control” Ph²TIP-based Fe(II) complex with a completely innocent ligand (i.e., one incapable of transferring either protons or electrons). For this purpose we selected 2-methoxy-5-methylphenolate (^{Me}2MP; Scheme 2); this ligand is structurally similar to ^tBuCatH, yet the second O-donor is methylated instead of protonated. Complex [Fe²⁺(Ph²TIP)(^{Me}2MP)]OTf, [5]OTf, was prepared in a manner similar to [3]OTf, and light green crystals were obtained by layering a CH₂Cl₂ solution with hexanes. The resulting structure reveals a 5C, high-spin Fe(II) center bound to Ph²TIP and ^{Me}2MP in a distorted trigonal-bipyramidal geometry (Supporting Information, Figure S2). Importantly, the Fe–O/N bond distances measured for [5]⁺ are very similar to those found for [3]⁺ (Table 2); like ^tBuCat, the ^{Me}2MP ligand binds in an asymmetric manner, with Fe–O distances of 1.92 and 2.23 Å. Thus, the overall structure of [5]⁺ closely resembles those in the *o*-phenylene series. However, methylation of the –OH donor eliminates the possibility of ligand-based electron transfer (ET) and proton transfer (PT), and this change causes the O₂ reactivities of [3]⁺ and [5]⁺ to diverge in dramatic fashion (vide infra).

Voltammetric studies of the Fe(II) complexes were conducted in CH₂Cl₂ at a scan rate of 100 mV/s with 0.1 M (NBu₄)PF₆ as the supporting electrolyte; redox potentials were referenced to ferrocenium/ferrocene (Fc^{+/0}). The CV of the catecholate complex [3]⁺ displays an irreversible anodic wave at +740 mV (Figure 3) and a quasi-reversible couple with E_{1/2} = –30 mV (peak-to-peak separation, ΔE, of 120 mV). Complex [5]⁺ exhibits a quasi-reversible event at nearly the same

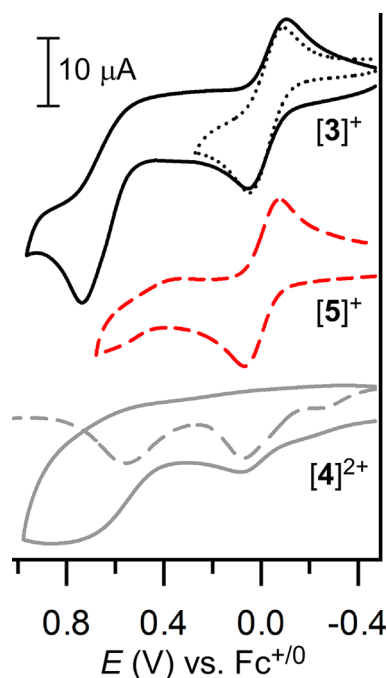


Figure 3. Cyclic voltammograms for [3]OTf (top, black), [5]OTf (middle, red), and [4](OTf)₂ (bottom, gray) collected in CH₂Cl₂ with 0.1 M (NBu₄)PF₆ as the supporting electrolyte and a scan rate of 100 mV/s. The corresponding square-wave voltammogram (dashed line) is also shown for [4](OTf)₂. In all cases the voltammogram was initiated by the anodic sweep.

potential (–10 mV, ΔE = 145 mV), consistent with the structural similarity between [3]⁺ and [5]⁺ noted above. In our previous electrochemical studies of high-spin 5C Fe(II) complexes with Tp or TIP ligands, the Fe²⁺/Fe³⁺ couple generally appears within 300 mV of the Fc^{+/0} reference.^{37,73,74} Thus, it is reasonable to assign the first oxidations of [3]⁺ and [5]²⁺ to the Fe²⁺/Fe³⁺ couple.

By comparison, the cyclic voltammogram of the phenylenediamine complex [4](OTf)₂ is less well-defined, but two events are clearly evident at +70 and 560 mV in the corresponding square-wave voltammogram (dashed line in Figure 3). We attribute the low-potential peak to the Fe²⁺/Fe³⁺ couple, which appears ~100 mV higher than the corresponding potentials for [3]⁺ and [5]⁺. This anodic shift is likely due to the neutral charge of ^tBuPDA compared to the monoanionic ^tBuCatH and ^{Me}2MP ligands. The high-potential redox events for [3]⁺ and [4]²⁺ arise from oxidation of the catecholate or phenylenediamine ligand, respectively. This assignment is consistent with a previous study by Lever et al., which found that the PDA ligand is oxidized at +500 mV when bound to a Ru(II) center.⁷⁵ Both redox events are irreversible for [4]²⁺; indeed, the electrochemical behavior of [4]²⁺ resembles that reported previously for the *o*-aminophenolate complex 1, which likewise exhibits an irreversible anodic wave near 0 mV, likely due to an ET–PT process.³⁷ For reasons that are not clear to us, complex [2]OTf failed to exhibit well-defined electrochemical features; however, on the basis of prior results,⁷³ the Fe²⁺/Fe³⁺ potential of [2]OTf is likely ~150 mV more positive than the corresponding potential of 1.

3.B. Reaction with Dioxygen. Pale yellow solutions of [3]OTf in CH₂Cl₂ undergo rapid color change upon exposure to air, yielding the blue-green chromophore 3^{ox}. The corresponding electronic absorption spectrum, shown in Figure 4, consists of two broad bands at 700 and 905 nm with ε-values of ~1100 M^{–1} cm^{–1}. These spectral features are characteristic of ferric-catecholate(2–) complexes and arise from ^tBuCat → Fe(III) ligand-to-metal charge transfer (LMCT) transitions.^{51,71,72} The EPR spectrum of 3^{ox} displays two S = 5/2 signals with E/D values of 0.14 and 0.25 (Supporting Information, Figure S3), consistent with the presence of a high-spin Fe(III) center. In addition, the Mossbauer (MB) spectrum of 3^{ox} reveals two quadrupole doublets with isomer shifts (δ) near 0.5 mm/s, typical of high-spin ferric ions (Table 3 and Supporting Information, Figure S4). The doublets have different splittings (ΔE_Q) of 0.82 and 1.24 mm/s. The heterogeneity in E/D and ΔE_Q values likely arises from different orientations of the ^tBuCat ligand in the oxidized complex, similar to the situation observed in the solid state for [3]OTf. Collectively, the spectroscopic data indicate that 3^{ox} has the formula of [Fe³⁺(Ph²TIP)(^tBuCat)]OTf.

In the presence of air, the distinctive absorption bands of 3^{ox} exhibit first-order decay with a half-life (t_{1/2}) of 6300 s, eventually yielding a nearly featureless spectrum. Previous studies of related complexes indicate that this decomposition corresponds to oxidation of the catecholate ligand via one (or more) of the pathways shown in Scheme 3.^{49,71,76} To determine reaction products, the final mixture was analyzed after treatment with acid and extraction into organic solvent (MeCN/Et₂O). The extradiol cleavage products, 4-*tert*-butyl-2-pyrone and 5-*tert*-butyl-2-pyrone, are generated in a 40:60 ratio with an overall yield of ~30%, as determined by ¹H NMR. These compounds were also observed using GC–MS, although the isomers are indistinguishable by this technique. When the

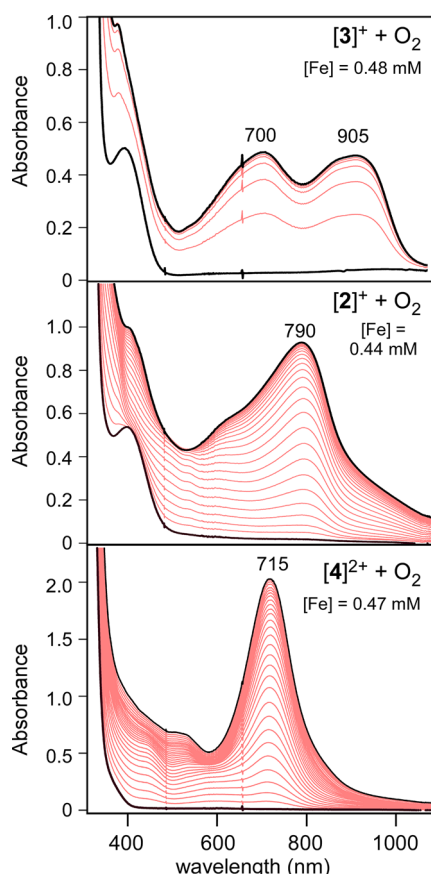


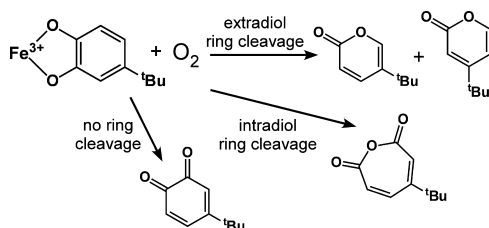
Figure 4. Time-resolved absorption spectra for the reaction of [3]OTf (top), [2]OTf (middle), and [4](OTf)₂ (bottom) with O₂; spectra were collected at intervals of 1, 20, and 14 400 s, respectively. Each reaction was performed at room-temperature in O₂-saturated CH₂Cl₂ ([O₂] = 5.8 mM). The path length of the cuvette was 1.0 cm.

Table 3. Experimental Mössbauer Parameters

complex	isomer shift (δ) mm/s	quadrupole splitting (ΔE_Q) mm/s	reference
1	1.06	2.52	32
[2]OTf	1.06 (70%)/1.14 (30%)	2.08/2.93	32
2 ^{ox}	0.64	1.94	32
[3]OTf	1.08	2.05	this work
3 ^{ox}	0.53/0.50	0.82/1.24	this work
[4](OTf) ₂	1.04 (75%)/1.05 (25%)	3.13/2.53	this work
4 ^{ox}	1.03 (40%)/1.18 (35%) ^a	1.98/3.24	this work

^aThe remaining intensity (25%) arises from the starting material, [4](OTf)₂.

Scheme 3



reaction was performed with ¹⁸O₂, the ion signal arising from the extradiol products shifted upward by two mass units, providing conclusive evidence for incorporation of one O atom from O₂ (Supporting Information, Figure S5). The 3^{ox} reactivity conforms to the previously established pattern that iron(III)-catecholate complexes with facial, tridentate supporting ligands yield primarily extradiol products, while those with tetradentate ligands provide intradiol products.^{50,51,77,78}

Interestingly, while [3]⁺ converts to 3^{ox} in a matter of seconds upon exposure to O₂, complex [5]⁺ is relatively stable in the presence of air. As shown in Supporting Information, Figure S6, the ¹H NMR spectrum of [5]⁺ in CD₂Cl₂ features paramagnetically shifted peaks at 58 and −10 ppm that arise from the ^{Me}2MP ligand. These peaks display only modest decreases in intensity (relative to an internal standard) after exposure to O₂ for several days, indicating that the geometric and electronic structures of [5]⁺ remain essentially intact in aerobic solution. UV–vis absorption spectra of [5]⁺ in O₂-saturated CH₂Cl₂ were collected over a span of 24 h (Supporting Information, Figure S7). These data revealed a gradual increase of absorption intensity in the 500–900 nm region, which corresponds to formation of the ferric complex, [Fe³⁺(^{Ph}2TIP)(^{Me}2MP)]²⁺ (5^{ox}). The absorption spectrum of 5^{ox} was measured independently by treating [5]⁺ with 1 equiv of an acetylferrocenium salt (Supporting Information, Figure S7). On the basis of these results, the conversion of [5]⁺ → 5^{ox} is only 20% complete after 24 h. The stark contrast in O₂ reactivities between [3]⁺ and [5]⁺ is remarkable given that the two complexes possess very similar geometric structures and Fe^{3+/2+} redox potentials.

As shown in Figure 4, reaction of the *o*-aminophenolate complex [2]OTf with O₂ at room temperature generates a green chromophore (2^{ox}) with absorption peaks at 790 and 420 nm. This spectrum is essentially identical to the one previously obtained by treating [2]OTf with 2 equiv of a one-electron oxidant (e.g., AgOTf).³⁷ Thus, it is reasonable to assume that 2^{ox} corresponds to [Fe(^{Ph}2TIP)(L_{O,N})]²⁺, where the electronic structure can be described as either Fe³⁺–^tBu₂ISQ or Fe²⁺–^tBu₂IBQ (vide supra). These results indicate that O₂ is capable of extracting two electrons from [2]⁺, whereas initial exposure of [3]⁺ to O₂ involves only one-electron oxidation of the complex. In both reactions, the ET process is associated with loss of a proton from the bidentate ligand. Similar to 3^{ox}, complex 2^{ox} undergoes decomposition in the presence of O₂, albeit at a much slower rate (*t*_{1/2} ≈ 18 h).

The *o*-phenylenediamine complex [4](OTf)₂ is comparatively less reactive toward O₂, requiring days (instead of minutes or hours) for complete oxidation. The resulting complex, 4^{ox}, displays an intense absorption band with λ_{max} = 715 nm (ϵ = 4300 M^{−1} cm^{−1}) and a weaker feature at ~500 nm (Figure 4). This deep-green species is air-stable at room temperature, allowing for crystallization from a MeCN/Et₂O mixture. Unfortunately, extensive disorder within the crystal has prevented the collection of a high-resolution structure. The crude crystallographic data indicate that 4^{ox} carries a +2 charge, based on the number of counteranions present. The complex is 5C with the ^tBuPDA-derived ligand bound in a bidentate manner, although sizable uncertainties in metric parameters preclude reliable evaluation of Fe or ligand oxidation states. Solutions of 4^{ox} are EPR silent with room-temperature magnetic moments of 5.14 μ_B , indicative of a *S* = 2 paramagnet. Since it was not possible to obtain a suitable X-ray crystal structure of 4^{ox}, we employed spectroscopic and computational

techniques to gain insight into its geometric and electronic structures, as described in the following section.

3.C. Spectroscopic and Computational Studies of 4^{ox}

3.C.i. Mössbauer Experiments. Low-temperature (5 K) MB spectra of $[4](\text{OTf})_2$ collected before and after exposure to O_2 are shown in Figure 5. The parameters obtained from fitting the

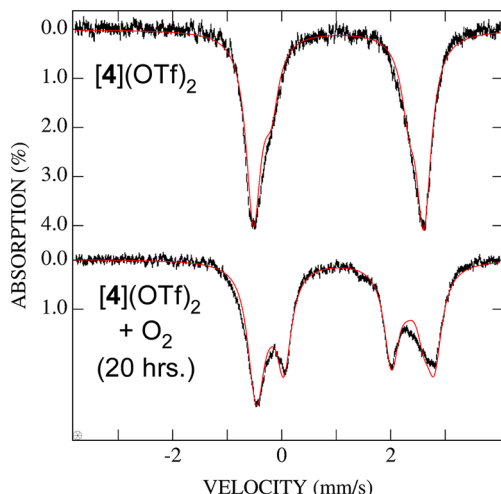


Figure 5. Mössbauer spectra collected before and after exposure of $[4](\text{OTf})_2$ to O_2 (top and bottom spectra, respectively). Both spectra were recorded at 5 K in an applied field of 0.04 T. The solid red lines are least-squares fits to the experimental data using the parameters in Table 3. Both spectra were fitted assuming nested doublets. Approximately 25% of the area in the spectrum of the O_2 -exposed sample (bottom) was ascribed to $[4](\text{OTf})_2$ starting material.

data are provided in Table 3. The major component (75%) of the $[4](\text{OTf})_2$ spectrum is a quadrupole doublet with an isomer shift (δ) of 1.04 mm/s and large splitting (ΔE_{Q}) of 3.1 mm/s. A minor feature (25%) is also evident with δ - and ΔE_{Q} -values of 1.05 and 2.5 mm/s, respectively. Both signals are characteristic of nonheme high-spin Fe(II) centers with N/O coordination. Given the nearly identical isomer shifts, the two doublets likely correspond to conformational isomers of $[4]^{2+}$ that adopt different geometries along the square-pyramidal to trigonal-bipyramidal continuum; indeed, similar “ τ -strain” was observed in our previous MB studies of $[2]\text{OTf}$.^{37,79} Upon exposure to O_2 for 20 h, new features arising from 4^{ox} become clearly evident (Figure 5), although starting material remains. Adequate fitting of the new signal required two equally intense doublets with $\delta = 1.03$ and 1.18 mm/s and $\Delta E_{\text{Q}} = 2.0$ and 3.2 mm/s (Table 3). As with $[4](\text{OTf})_2$, the observed heterogeneity is likely due to minor changes in coordination geometries. Significantly, the MB data provide conclusive proof that the conversion of $[4]^{2+}$ to 4^{ox} by O_2 does not involve oxidation of the Fe center, as the isomer shifts remain above 1.0 mm/s in the final complex.

With the MB data in hand, it is now possible to determine the oxidation state of the $^{\text{tBu}}$ PDA-derived ligand in 4^{ox} . Since the overall complex has a +2 charge, the ligand itself must be neutral; thus, two possibilities exist: (diimino)-benzosemiquinone radical or (diimino)benzoquinone ($^{\text{tBu}}$ DIBQ). The former possibility is inconsistent with the EPR-silent nature of 4^{ox} and its magnetic moment of 5.14 μ_{B} . Therefore, 4^{ox} is best formulated as $[\text{Fe}^{2+}(\text{Ph}_2\text{TIP})-(^{\text{tBu}}\text{DIBQ})]^{2+}$ —a conclusion further supported by the DFT and rR results described below. Similar to $[2]^+$, complex $[4]^{2+}$ is

oxidized by two electrons upon exposure to O_2 , although in the PDA system the electrons are derived exclusively from the ligand, and two protons are removed.

Table 3 summarizes the MB parameters reported here (and previously) for complexes $1-[4]^{2+}$ and their X^{ox} counterparts. The electronic structures of the Fe(II) precursors are quite similar, with isomer shifts of $\delta = 1.09 \pm 0.05$ mm/s and ΔE_{Q} values between 2.05 and 3.13 mm/s. In contrast, there is considerable variation in the X^{ox} parameters. Isomer shifts for 3^{ox} and 4^{ox} are characteristic of high-spin ferric and ferrous ions, respectively, whereas the δ value of 2^{ox} (0.64 mm/s) precludes an unambiguous assignment of oxidation state, as noted above. Significantly, the MB results reveal that the redox chemistry of these complexes spans the entire gamut from iron-based to ligand-based oxidations.

3.C.ii. DFT Calculations of 4^{ox} . Following the experimental data, the geometry optimization of 4^{ox} assumed a 5C geometry, $S = 2$ ground state, and overall charge of +2. Metric parameters for the resulting model (4^{ox} -DFT) are provided in Figure 6.

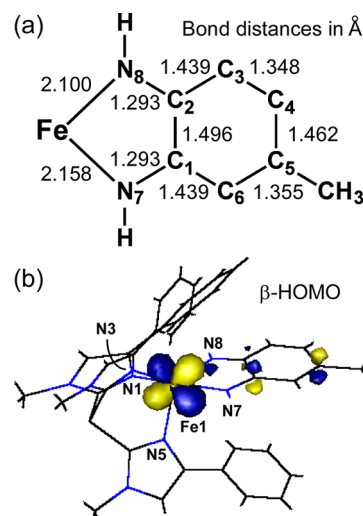


Figure 6. (a) Bond distances (in Å) of the $[\text{Fe}(\text{DIBQ})]^{2+}$ unit in the 4^{ox} -DFT model. (b) Isosurface plot of the spin-down (β) HOMO of 4^{ox} -DFT.

The short N–C bond distances of 1.29 Å and “four long/two short” pattern of C–C bonds in the N,N -ligand are well-established characteristics of DIBQ units.^{3,30,80–83} Mulliken populations revealed that spin-density is found almost exclusively on the Fe center (3.88 α spins), while the bidentate ligand is largely devoid of unpaired spin. The most relevant molecular orbital (MO) for evaluating the 4^{ox} -DFT electronic configuration is the highest-occupied (HO) spin-down (β) MO, shown in Figure 6. The character of this MO is 74% Fe and 14% N,N -ligand, with electron density mainly found in a 3d orbital that bisects the N7–Fe1–N8 angle. Thus, there is only modest transfer of electron density from the Fe(II) center to the $^{\text{tBu}}$ DIBQ ligand, in agreement with the MB data presented above.

To aid in band assignments, the absorption spectrum of 4^{ox} -DFT was calculated using TD-DFT. As shown in Supporting Information, Figure S8, the computed spectrum exhibits two bands at 635 and 460 nm ($\epsilon = 5.4$ and 2.2 $\text{M}^{-1} \text{cm}^{-1}$, respectively) that correspond to features in the experimental spectrum. The higher-energy band arises primarily from a $^{\text{tBu}}$ DIBQ-based π – π^* transition, as revealed in the electron

density difference map (EDDM; Supporting Information, Figure S8). In contrast, the intense near-IR (NIR) band corresponds to an Fe(II) \rightarrow tBu DIBQ MLCT transition localized on the N7–Fe1–N8 unit.

3.C.iii. Resonance Raman Experiments. The electronic structure of the tBu PDA-derived ligand in 4^{ox} was further examined using resonance Raman (rR) spectroscopy. Since the complex exhibits a pair of prominent absorption bands, data were collected with two wavelengths of excitation (λ_{ex}): 647.1 nm light from a Kr⁺ laser was used to probe the NIR feature that arises from a MLCT transition, while 488.0 nm light from an Ar⁺ laser was selected to resonate with the tBu DIBQ-based π – π^* transition. The composite spectrum, shown in Figure 7,

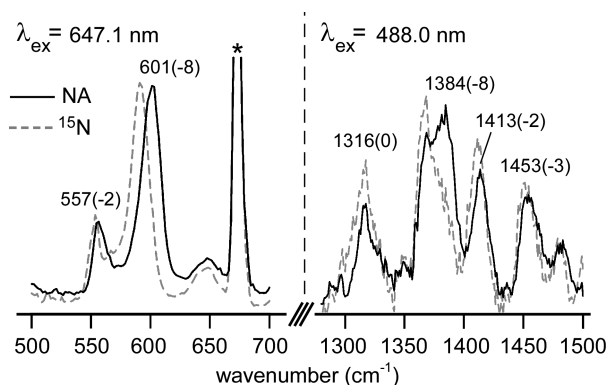


Figure 7. Resonance Raman spectra of 4^{ox} in frozen CD_2Cl_2 solutions ($[Fe] = 7.8$ mM) collected with 647.1 nm (left) and 488.0 nm (right) laser excitation. The black (solid) spectra were obtained using natural abundance (NA) complex, while the gray (dashed) spectra were obtained using ^{15}N -substituted complex (the ^{15}N isotope was incorporated at the 2-position of the PDA ligand). Frequencies (in cm^{-1}) are provided for select peaks in the NA spectra, and the corresponding $^{14}N \rightarrow ^{15}N$ shifts are shown in parentheses. Peaks marked with an asterisk (*) arise from frozen solvent.

was obtained by irradiating frozen samples of 4^{ox} in CD_2Cl_2 . In some samples, the bidentate N,N -ligand was labeled with the ^{15}N isotope at the 2-position to aid in peak assignments.

The low-frequency region of the 4^{ox} spectrum features two intense peaks at 557 and 601 cm^{-1} with ^{15}N isotope shifts of 2 and 8 cm^{-1} , respectively (Figure 7). The 601 cm^{-1} peak is attributed to the breathing mode of the five-membered FeN_2C_2 chelate ring, based on its intensity and sizable isotope shift. This assignment is supported by literature precedents^{84–86} and DFT frequency calculations performed with the 4^{ox} -DFT model (computed frequencies and normal mode compositions are provided in Supporting Information, Figure S9). The smaller isotope shift of the 557 cm^{-1} peak suggests that the corresponding normal mode involves substantial mixing of Fe–N stretching motions with internal C–N/C–C vibrations of the bidentate ligand. Both modes are strongly enhanced by excitation into the NIR band at 715 nm, consistent with its assignment as an Fe(II) \rightarrow tBu DIBQ MLCT transition.

Compared to the metallocycle-based features, peaks arising from ligand-based modes ($\nu \cong 1200$ – 1600 cm^{-1}) are quite weak in the 4^{ox} spectrum obtained with $\lambda_{ex} = 647.1$ nm. However, the higher-energy peaks gain in relative intensity when λ_{ex} is changed to 488.0 nm, providing further confirmation that the absorption manifold near 500 nm arises from tBu DIBQ-based transitions. Three isotopically sensitive peaks are apparent at 1384, 1413, and 1453 cm^{-1} (Figure 7).

Prior rR studies of metal-dioxolene complexes indicate that these peaks correspond to modes that couple $\nu(N-C)$ and $\nu(C-C)$ motions within the bidentate N,N -ligand.^{84–86} On the basis of its large ^{15}N isotope shift (8 cm^{-1}), the experimental peak at 1384 cm^{-1} matches the DFT-computed mode at 1372 cm^{-1} , which has primarily $\nu(N-C)$ character (calculated ^{15}N isotope shift of 7 cm^{-1} ; Supporting Information, Figure S9). The peaks at 1413 and 1453 cm^{-1} then correspond to $\nu(C-C)$ motions of the tBu DIBQ ring with only minor amounts of $\nu(N-C)$ character. Similarly, Lever and co-workers recently published the crystal structure and rR spectrum of $[Ru^{3+}Cl_2(NH_3)_2(DIBQ)]^+$, where DIBQ is unsubstituted (diimino)-benzoquinone.⁸⁶ This complex displays three peaks between 1400 and 1500 cm^{-1} that the authors attribute to stretching modes of the DIBQ ligand. The presence of resonance-enhanced peaks at similar frequencies in the 4^{ox} spectrum provides further evidence that this complex contains a tBu DIBQ ligand.

3.D. Kinetic Analysis of O_2 Reactivity. Kinetic studies were generally conducted in O_2 -saturated CH_2Cl_2 solutions ($[O_2] = 5.8$ mM at 20 $^{\circ}C$ ^{41,42}), and rates were measured by monitoring the growth of absorption features associated with the X^{ox} species. To ensure a large excess of O_2 , concentrations of the Fe(II) complexes never exceeded 1.0 mM. For the reactions of $[2]^+$ and $[3]^+$ with O_2 , initial rates increased linearly with Fe and O_2 concentrations, indicating that the reactions are first-order in both reactants (Supporting Information, Figures S10 and S11). Interestingly, while the $[4]^{2+} + O_2$ reaction is also first-order in Fe concentration, the reaction rate displays only minor variations as $[O_2]$ increases from 0.2 to 5.4 mM (Supporting Information, Figure S11). This zero-order $[O_2]$ dependence indicates that O_2 binding is not the rate-limiting step in the conversion of $[4]^{2+} \rightarrow 4^{ox}$.

As shown in Figure 8, the reaction of $[3]OTf$ with O_2 at ambient temperature proceeds via pseudo-first-order kinetics with a rate constant (k_1) of 0.67(5) s^{-1} . The formation of 2^{ox} and 4^{ox} under the same conditions is more complex, however, as indicated by the “S-shaped” kinetic traces (Figure 8). This behavior suggests that these species are generated via multistep mechanisms involving both ET and PT—a common occurrence for reactions that require net hydride (2^{ox}) or H_2 transfer (4^{ox}).^{87,88} Because of this mechanistic complexity, k_1 values for the reactions of O_2 with $[2]^+$ and $[4]^{2+}$ were measured using the initial rates approach. Interestingly, the rates of formation span more than 5 orders of magnitude, with k_1 values of 0.67(5) (3^{ox}), $1.3(2) \times 10^{-3}$ (2^{ox}), and $4(2) \times 10^{-6}$ s^{-1} (4^{ox}) in O_2 -saturated CH_2Cl_2 at room temperature. We also measured an initial rate of 5×10^{-6} s^{-1} for the one-electron oxidation of $[5]^+$ to 5^{ox} (Supporting Information, Figure S7). Thus, despite similar structures, the complexes examined here differ dramatically in their O_2 reactivities.

Activation parameters for the $[2]OTf + O_2$ reaction were determined by measuring rates at temperatures between 22 and -30 $^{\circ}C$. The linear Eyring plot (Supporting Information, Figure S12) indicates an activation enthalpy (ΔH^\ddagger) of 12(2) $kcal \cdot mol^{-1}$ and a large negative activation entropy (ΔS^\ddagger) of $-22(5)$ $cal \cdot mol^{-1} \cdot K^{-1}$. Such values are similar to parameters obtained for similar Fe/ O_2 adducts^{46,89} and are consistent with an associative reaction involving O_2 binding to the Fe center as the rate-determining step.

3.E. Reaction with H-atom Acceptors. In previous sections, we demonstrated that formation of the oxidized species 2^{ox} – 4^{ox} under aerobic conditions requires both electron

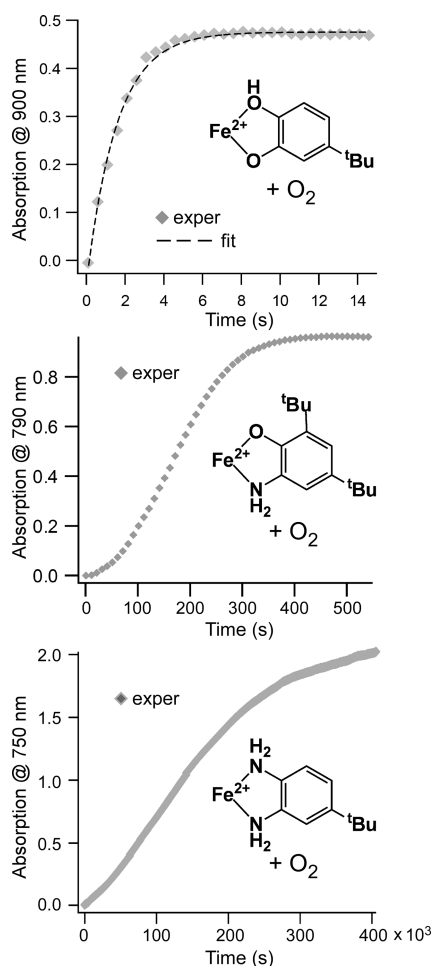


Figure 8. Plots of absorption intensity as a function of time for the reactions of [3]OTf (top), [2]OTf (middle), and [4](OTf)₂ (bottom) with O₂. All reactions were performed in O₂-saturated CH₂Cl₂ at room temperature ([Fe] ≈ 0.50 mM).

and proton transfers from the parent complexes, although the rates of O₂ reaction vary by a factor of 10⁵ across the series. Thus, it is plausible that the O₂ activation mechanisms involve a combination of electron *and* proton transfer from the complexes to either dioxygen or superoxide. We therefore examined the reactivity of the title complexes with two well-established H-atom acceptors: TEMPO[•] and 2,4,6-tri-*tert*-butylphenoxyl radical (TTBP[•]). Both reagents exhibit a strong propensity to react via PCET mechanisms, but TTBP[•] is a much more effective H-atom abstractor than TEMPO[•], as indicated by the bond dissociation free energies (BDFE) of the resulting H–O bonds (BDFE = 77.1 and 66.5 kcal/mol, respectively, in MeCN).⁹⁰

Treatment of [3]⁺ with either TEMPO[•] or TTBP[•] yields a blue-green species with absorption features identical to those observed for 3^{ox} (Supporting Information, Figure S13). Given the formulation of 3^{ox} as [Fe³⁺(Cat)(Ph₂TIP)]⁺, this reaction is classified as “separated PCET” because the electron and proton originate from different units of the [3]⁺ complex, namely, the Fe(II) center and CatH ligand. While complexes [2]⁺ and [4]²⁺ are inert toward TEMPO[•], both react rapidly with TTBP[•]. As described in a previous manuscript,³⁷ TTBP[•] removes a hydrogen atom from the ^{*t*}Bu₂APH ligand of [2]⁺ to generate the corresponding Fe(II)–^{*t*}Bu₂ISQ complex. Complex [4]²⁺ reacts with 2 equiv of TTBP[•] to provide a species with

spectral features that are similar to those of 4^{ox}, although not identical (Supporting Information, Figure S14). This chromophore is evident by UV–vis spectroscopy even when a single equivalent of TTBP[•] is added; this result suggests that the species generated by removal of one H-atom from [4]²⁺ undergoes disproportionation to yield the starting complex and a 4^{ox}-like species.

It is noteworthy that [3]⁺ is the only complex in the series capable of donating a H-atom to TEMPO[•], indicating that the [3^{ox}–H] bond is very weak (BDFE < 66 kcal/mol). Bordwell and Mayer have demonstrated that the BDFE the X–H bond formed in a 1H⁺/1e[−] PCET reaction (i.e., X[•] + H⁺ + e[−] → X–H) is given by the following equation:

$$\text{BDFE}(\text{X} - \text{H}) = 1.37\text{p}K_{\text{a}} + 23.06E^{\circ} + C_{\text{G,solv}}$$

where $C_{\text{G,solv}}$ is a solvent-dependent constant.^{90,91} In our case, the relevant parameters are the E° values of the starting Fe(II) complexes and the $\text{p}K_{\text{a}}$ values of the one-electron oxidized species. The complexes examined here exhibit greater variability in ligand acidities than in redox potentials. As described above, initial redox potentials differ by ~100 mV across the series, accounting for a modest shift of ~2.5 kcal/mol in BDFE. In contrast, the $\text{p}K_{\text{a}}$ values of aromatic amines are generally ~12 units higher than the corresponding phenols—a shift of 14 kcal/mol in BDFE.^{90,92,93} Thus, while the differences in redox potential cannot be ignored, the weaker H-atom donating ability of complexes [2]⁺ and [4]²⁺ compared to [3]⁺ is largely due to the greater acidity of the ^{*t*}BuCatH ligand relative to ^{*t*}Bu₂APH and ^{*t*}BuPDA.

These results have mechanistic implications for the O₂ reactivity of the complexes examined here. The strength of the [3^{ox}–H] bond is comparable to that of perhydroxyl radical (HO₂[•]), which is the product of HAT and O₂ (BDFE of HO₂[•] ≈ 60 kcal/mol).⁹⁰ Therefore, complex [3]⁺ may be able to react directly with O₂ via 1H⁺/1e[−] PCET *without prior formation of a ferric-superoxo intermediate*. By contrast, complexes [2]⁺ and [4]²⁺ cannot participate in HAT reactions with O₂ due to the greater strength of their N–H bonds. For these complexes, O₂ activation likely requires initial ET from Fe(II)→O₂, followed by oxidation of the ligand via concerted (or stepwise) electron and proton transfers. These mechanistic scenarios are considered further in the Discussion section.

3.F. Computational Studies of O₂ Reactivity. The thermodynamics of O₂ binding were examined with DFT calculations. A previous study by Schenk et al. found that hybrid functionals with a reduced amount (~10%) of Hartree–Fock (HF) exchange are most reliable for evaluating the energetics of O₂ (or NO) binding to nonheme Fe(II) centers.⁹⁴ We therefore employed the PBE functional⁶⁵ with 10% HF exchange to calculate geometries and thermodynamic parameters for O₂, the Fe(II) precursors, and the 6C [Fe/O₂] adducts. Since exchange interactions between the unpaired electrons of Fe and O₂ give rise to three possible spin states ($S_{\text{tot}} = 1, 2, 3$), it was necessary to optimize three models for each [Fe/O₂] species. The resulting $S = 2$ [Fe/O₂] structures are shown in Figure 9. (Supporting Information, Tables S1–S3 provide metric parameters for each model.) The [4/O₂]²⁺ adduct is dissociative on the $S = 3$ surface, with calculations invariably converging to structures with very long Fe...O distances (>3.75 Å). In all other cases, O₂ coordinates in a bent conformation with Fe–O–O angles between 120 and 140° and Fe–O distances ranging from 1.95 to 2.18 Å. The O₂ ligand can adopt two possible orientations depending on whether the O–

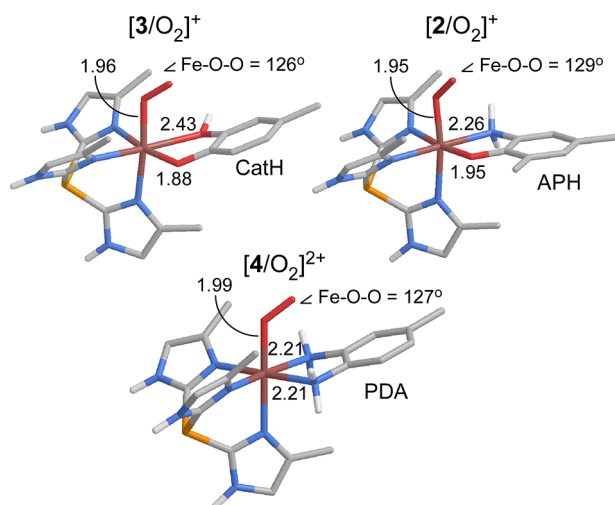


Figure 9. DFT-calculated structures of the Fe/O₂ adducts. Selected bond distances (Å) and angles are provided (see Supporting Information, Tables S1–S3 for additional metric parameters).

O vector is pointed toward (T) or away (A) from the bidentate ligand. The two orientations are approximately isoenergetic with differences less than the estimated error of the calculations (± 2 kcal/mol). In the remainder of this Paper, only the T isomers of the [Fe/O₂] adducts are discussed, since these models are more relevant from a mechanistic standpoint.

Table 4 summarizes the computed thermodynamic parameters for the eight Fe(II) + O₂ → [Fe/O₂] reactions considered here. While the enthalpic contributions ($\Delta H^{\text{gas}} + \Delta \text{Solv}$) are slightly favorable in most instances, all of the reactions are endergonic ($\Delta G = +7.0$ – 13.0 kcal/mol) due to large and unfavorable entropic effects. A similar pattern has been observed in DFT studies of O₂ binding to nonheme Fe(II) enzymes, where the calculated ΔG values range between +8 and 12 kcal/mol.^{95–98} To understand why the O₂ binding reactions are decidedly “uphill,” it is instructive to examine the computed properties of the O–O bonds in the [Fe/O₂] intermediates. Superoxide ligands typically exhibit O–O bond distances near 1.3 Å and $\nu(\text{O–O})$ frequencies between 1050 and 1200 cm^{−1}.⁹⁹ In contrast, our DFT-generated [Fe/O₂] models have short O–O distances of 1.25 ± 0.02 Å and $\nu(\text{O–O})$ frequencies greater than 1250 cm^{−1} (Table 4), indicating that there is only partial charge transfer from Fe(II) to the O₂ ligand. The weakness of the Fe–O₂ interactions is also reflected in the low $\nu(\text{Fe–O})$ frequencies, which range between 230 to 370 cm^{−1}.

On the basis of the DFT calculations, complex [2]⁺ has the greatest affinity for O₂, followed in the series by [3]⁺ and [4]²⁺ (Table 4). This trend correlates with the relative donor strengths of the bidentate ligands (APH[−] > Cath[−] > PDA) because formation of the Fe–O₂ bond requires transfer of electron density from an Fe d orbital to an empty O₂ π^* orbital. However, our DFT results appear to contradict the kinetic studies reported above, which found that [3]⁺ is significantly more reactive than [2]⁺ toward O₂. Possible explanations for this discrepancy are provided in the following section.

4. DISCUSSION

In this Manuscript, we described the O₂ reactivity of monoiron(II) complexes bound to three types of *o*-phenylene ligands (Schemes 1 and 2). The complexes resemble the substrate-bound intermediates of nonheme Fe(II) dioxygenases that catalyze the oxidative ring-cleavage of aromatic substrates.^{32–34} The ^{Ph}₂TIP supporting ligand mimics the facial triad of protein ligands in the active site and the substrate ligands each coordinate in a bidentate manner, resulting in 5C Fe(II) complexes capable of O₂ binding. In an earlier study, we demonstrated that one- and two-electron oxidation of the ^tBu₂APH-based complex [2]OTf yields species containing (imino)benzosemiquinone ligands.³⁷ Like aminophenolates, catecholates and phenylenediamines can serve as redox-active ligands, although the ease of oxidation of the free ligands increases across the series Cath₂ < APH₂ < PDA. We therefore synthesized and structurally characterized the homologous complexes [3]OTf and [4](OTf)₂ to better understand the role of redox-active ligands in modulating the O₂ reactivity of Fe complexes. The ligands are capable of donating protons as well as electrons, but the acidities run counter to the redox potentials. In other words, the most acidic ligand (^tBu₂Cath₂) is the hardest to oxidize, while the most reducing ligand (^tBu₂PDA) is the least acidic. This interplay between ET and PT capabilities influences the rates of the O₂ reactions as well as the identities of the oxidized products.

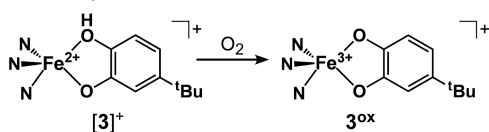
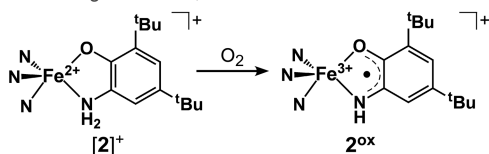
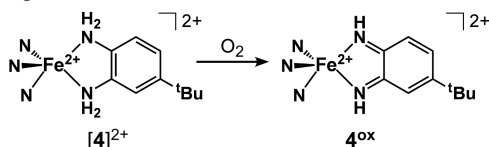
Despite similar overall structures, the three Fe(II) complexes in this study display remarkable diversity in their O₂ reactivities, as summarized in Scheme 4. The differences concern both the total number of electrons transferred in the reaction (1e[−] or 2e[−]) and the source of these electrons (iron and/or ligand). The resulting X^{ox} species have been characterized by various spectroscopic (UV–vis, EPR, MB, rR) and computational (DFT) methods. These results indicate that the [3]⁺ → 3^{ox} conversion is an Fe-based 1e[−] process, while the [4]²⁺ → 4^{ox} reaction involves 2e[−] oxidation of the ligand only. The [2]⁺ → 2^{ox} reaction occupies an intermediate position, since substantial

Table 4. Energetics of O₂ Binding to Complexes [2]⁺, [3]⁺, and [4]²⁺, and Comparison of O–O Bond Distances and Stretching Frequencies in the Resulting Fe/O₂ Adducts^a

reactants	spin (<i>S</i> _{tot})	ΔH^{gas}	<i>T</i> Δ <i>S</i>	ΔSolv^b	ΔG^c	<i>r</i> (O–O) (Å)	$\nu(\text{O–O})$ (cm ^{−1})
[3] ⁺ + O ₂	<i>S</i> = 3	−0.5	−11.9	−0.1	+11.3	1.25	1287
	<i>S</i> = 2	−0.2	−12.2	−1.1	+10.9	1.27	1260
	<i>S</i> = 1	−1.6	−11.7	+0.2	+10.3	1.25	1287
[2] ⁺ + O ₂	<i>S</i> = 3	−2.0	−10.0	−1.1	+6.9	1.26	1254
	<i>S</i> = 2	−1.4	−10.9	−1.7	+7.8	1.27	1251
	<i>S</i> = 1	−2.9	−11.4	−0.2	+8.3	1.25	1303
[4] ²⁺ + O ₂	<i>S</i> = 2	+4.0	−11.3	−2.3	+13.0	1.25	1328
	<i>S</i> = 1	−1.8	−12.2	+0.4	+10.8	1.23	1406

^aAll energies in kcal/mol. ^bEnthalpies of solvation were calculated using COSMO. ^c $\Delta G = \Delta H^{\text{gas}} + \Delta \text{Solv} - T\Delta S$

Scheme 4

Fe-based, 1e[−] oxidation:Fe- and ligand-based, 2e[−] oxidation:Ligand-based, 2e[−] oxidation:

electron density is lost from both the Fe center and ^tBu₂AP ligand. This continuum in electronic structures is evident in the isomer shifts (δ) of the X^{ox} species (Table 3), which range from 0.50 (3^{ox}, Fe³⁺) to 0.64 (2^{ox}, Fe^{2.5+}) to ~1.1 (4^{ox}, Fe²⁺) mm/s. In addition, each of the three possible *o*-phenylene oxidation states (aromatic, semiquinone, benzoquinone; Scheme 1) is represented in the X^{ox} series. Thus, the [Fe²⁺(^{Ph}₂TIP)](*o*-phenylene)] framework supports a wide spectrum of redox and O₂ chemistry.

Our kinetic analysis revealed that O₂ reaction rates vary by a factor of 10⁵ across the series, following the order [3]⁺ > [2]⁺ > [4]²⁺. It is somewhat counterintuitive that this order is *inversely* related to the electron-donating abilities of the free ligands. Moreover, these rates fail to correlate adequately with Fe^{2+/3+} redox potentials, all of which fall within a 100 mV range near 0 mV (vs Fc^{+/0}). Finally, if one assumes that formation of the Fe/O₂ adduct is the rate-determining step, then our DFT calculations of O₂-binding affinities indicate that [2]⁺ should be more reactive than [3]⁺, even though the kinetic data indicate that the reverse is true.

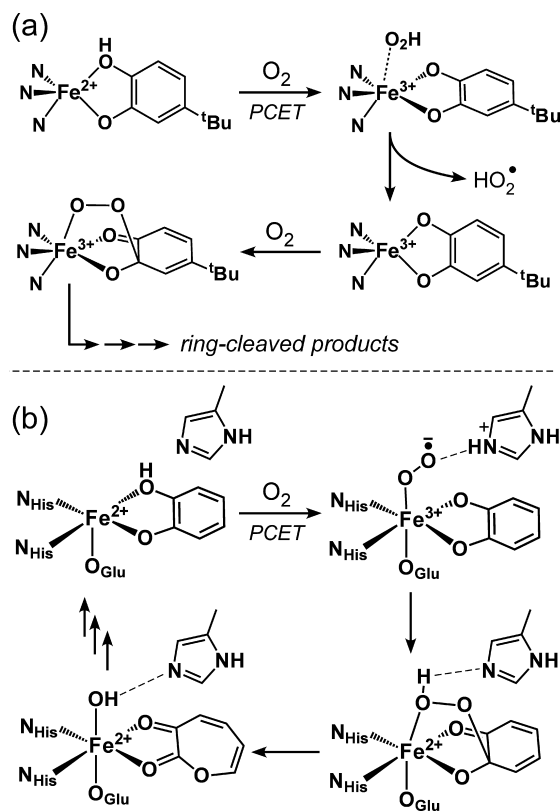
We believe these conflicting results can be reconciled by considering the role of PT in the O₂ reaction. The fact that [3]⁺ undergoes HAT with TEMPO—a very weak H-atom acceptor—suggests that ET and PT processes are tightly coupled in the [3]⁺ + O₂ reaction. A likely mechanism involves concerted transfer of 1e[−] and 1H⁺ to O₂ as it approaches the Fe center. In contrast, the intrinsically lower acidity of aromatic amines (relative to phenols) prevents PT in the initial interaction of O₂ with [2]⁺ and [4]²⁺. Deprotonation of these ligands in the course of the O₂ reaction likely requires complete oxidation of the Fe center to lower the pK_a of the amino group(s). Thus, these complexes cannot avoid the thermodynamically uphill ET from Fe(II) to O₂; yet once the ferric complex is generated, proton loss to superoxide or bulk solvent would be feasible, as indicated by the CV data (vide supra). Importantly, deprotonation destabilizes the redox-active MOs of the ligand, making it possible for O₂ to extract a second electron, thus generating the final 2^{ox} and 4^{ox} products. Thus, we propose that the [2]⁺ → 2^{ox} conversion proceeds via a stepwise ET–PT–ET mechanism, although PT may be coupled with the second ET in a HAT reaction. This mechanism follows the one established by Paine et al. for the oxidation of [Fe²⁺(L)](^tBu₂APH) to

[Fe³⁺(L)](^tBu₂ISQ)⁺ in the presence of O₂ (where L is the tris(2-pyridylthio)methanido anion).⁴⁸

The enormous contrast between the O₂ reactivities of [3]⁺ and [5]⁺ provides the clearest evidence for the decisive role of PT in determining reaction rates of the *o*-phenylene complexes. These two complexes have nearly identical coordination geometries and Fe^{3+/2+} redox potentials; however, replacing the –OH group of ^tBuCatH with the –OCH₃ donor of ^{Me}₂MP decreases the O₂ reaction rate by 5 orders of magnitude. Indeed, complex [5]⁺ is quite stable in the presence of air, even though slow oxidation to the ferric analog (5^{ox}) is observed over the course of days. These results provide further confirmation that the one-electron oxidation of high-spin Fe(II) centers by O₂ is an unfavorable process, but the overall reaction barrier can be lowered substantially if the ET is coupled with PT (in either a stepwise or concerted manner).

The 3^{ox} intermediate reacts further with O₂ to yield products arising from extradiol ring cleavage. Previous studies have proposed a mechanism that involves direct reaction of the [Fe³⁺(Cat)]⁺ unit with O₂ to form a ferric-alkylperoxy species, followed by rearrangement to the corresponding lactone (Scheme 5a).^{49,76} In contrast, 2^{ox} and 4^{ox} are relatively air-

Scheme 5



stable, since they lack the two reducing equivalents necessary to generate the critical alkylperoxy intermediate. Interestingly, Paine and co-workers recently reported a 6C complex, [Fe²⁺(6-Me₃-TPA)](^tBuAPH)⁺, that (unlike [2]⁺) reacts with O₂ to yield the ring-cleaved product (6-Me₃-TPA = tris(6-methyl-2-pyridylmethyl)amine).¹⁰⁰ The proposed mechanism is analogous to the one employed by ferric-catecholate complexes. Paine's system differs from the one described here in that the initial product of the O₂ reaction is an [Fe³⁺(AP)]⁺ species, whereas our previous studies indicate that [2]⁺ likely converts

to a $[\text{Fe}^{2+}(\text{ISQ})]$ intermediate. This difference in electronic structure apparently controls subsequent reactivity, with the latter species undergoing simple $1e^-$ oxidation and the former direct addition of O_2 .

The results presented here highlight the mechanistic sophistication of the ring-cleaving dioxygenases. Scheme 5b provides a condensed version of the canonical enzymatic mechanism. A recent DFT study by Christian et al. of extradiol catechol dioxygenases has emphasized the role of the conserved second-sphere histidine residue in the PT steps that occur after O_2 binding.⁹⁸ This residue first deprotonates the substrate ligand, resulting in an imidazolium group that stabilizes the superoxide ligand through H-bonding interactions. The proton is eventually returned to the O_2 unit after formation of the bridging alkylperoxo intermediate (Scheme 5b). Thus, the enzyme carefully “manages” the PT events to promote O_2 activation and discourage the autoxidation processes observed in our models. Indeed, studies of homoprotocatechuate 2,3-dioxygenase (HPCD) have demonstrated that if the His200 residue is mutated to Ala, the enzyme generates quinone and H_2O_2 instead of the ring-cleaved products.¹⁰¹ Therefore, the critical difference between the ring-cleaving dioxygenases and the synthetic models reported here (and elsewhere) is the ability to coordinate PT with O_2 activation.

It is noteworthy that none of the synthetic dioxygenase models prepared to date follow the enzymatic mechanism in proceeding through an Fe/O_2 adduct. Even for those complexes that carry out ligand cleavage, like $[\text{3}]\text{OTf}$, the first step always involves $1e^-$ oxidation to the ferric complex followed by direct reaction of the ligand with O_2 . The enzyme not only stabilizes the $[\text{FeO}_2]$ adduct through H-bonding interactions, it also prevents formation of the dead-end intermediate that arises when the substrate proton is transferred to $\text{O}_2^{\bullet-}$ instead of H200.^{101,102} In this study, we have shown that PCET is an effective strategy for bypassing the unfavorable ET from $\text{Fe}(\text{II})$ to O_2 ; however, in the case of $[\text{3}]\text{OTf}$, the PCET reaction does not lead to formation of the $\text{Fe}(\text{II})$ -alkylperoxo intermediate (as in the enzyme) because the resulting superoxide moiety has been deactivated through protonation. By coupling O_2 binding with PT to a second-sphere His residue, the dioxygenases reap the energetic benefits of PCET while avoiding the pitfall that has plagued synthetic models. Future modeling efforts should therefore be directed toward the generation of complexes capable of mimicking the enzyme's exquisite control of PT reactions.

■ ASSOCIATED CONTENT

■ Supporting Information

^1H NMR spectra of the $\text{Fe}(\text{II})$ complexes, crystallographic structure of $[\text{5}]\text{OTf}$, EPR and Mössbauer data for $[\text{3}]\text{OTf}$ and 3^{ox} , results from TD-DFT and frequency calculations of 4^{ox} , plots of initial rates versus $\text{Fe}(\text{II})$ and O_2 concentrations, Eyring plot for the reaction of $[\text{2}]\text{OTf}$ with O_2 , absorption spectra of the reactions of $[\text{3}]\text{OTf}$ and $[\text{4}](\text{OTf})_2$ with organic radicals, metric parameters for DFT-optimized models, and crystallographic data in CIF format. This material is available free of charge via the Internet at <http://pubs.acs.org>.

■ AUTHOR INFORMATION

Corresponding Authors

*E-mail: adam.fiedler@marquette.edu. (A.T.F.)

*E-mail: cpopescu@ursinus.edu. (C.V.P.) Fax: (+1) 414-288-7066.

Notes

The authors declare no competing financial interest.

■ ACKNOWLEDGMENTS

We thank Dr. Brian Bennett for allowing us to measure EPR data at the National Biomedical EPR Center (supported by NIH P41 Grant EB001980), and Thomas Brunold (Univ. Wisconsin–Madison) for access to his resonance Raman instrument. This research is generously supported by the National Science Foundation (CAREER CHE-1056845 to A.T.F., CHE-0956779 to C.V.P.).

■ REFERENCES

- (1) Kaim, W. *Inorg. Chem.* **2011**, *50*, 9752–9765.
- (2) Kaim, W. *Eur. J. Inorg. Chem.* **2012**, *2012*, 343–348.
- (3) Agarwala, H.; Ehret, F.; Chowdhury, A. D.; Maji, S.; Mobin, S. M.; Kaim, W.; Lahiri, G. K. *Dalton Trans.* **2013**, *42*, 3721–3734.
- (4) Das, D.; Sarkar, B.; Kumbhakar, D.; Mondal, T. K.; Mobin, S. M.; Fiedler, J.; Urbanos, F. A.; Jimenez-Aparicio, R.; Kaim, W.; Lahiri, G. K. *Chem.—Eur. J.* **2011**, *17*, 11030–11040.
- (5) Das, D.; Das, A. K.; Sarkar, B.; Mondal, T. K.; Mobin, S. M.; Fiedler, J.; Zalis, S.; Urbanos, F. A.; Jimenez-Aparicio, R.; Kaim, W.; Lahiri, G. K. *Inorg. Chem.* **2009**, *48*, 11853–11864.
- (6) Das, A. K.; Sarkar, B.; Duboc, C.; Strobel, S.; Fiedler, J.; Zalis, S.; Lahiri, G. K.; Kaim, W. *Angew. Chem., Int. Ed.* **2009**, *48*, 4242–4245.
- (7) Pierpont, C. G. *Inorg. Chem.* **2011**, *50*, 9766–9772.
- (8) Pierpont, C. G. *Coord. Chem. Rev.* **2001**, *219*, 415–433.
- (9) Brown, S. N. *Inorg. Chem.* **2012**, *51*, 1251–1260.
- (10) Poddel'sky, A. I.; Cherkasov, V. K.; Abakumov, G. A. *Coord. Chem. Rev.* **2009**, *253*, 291–324.
- (11) Munha, R. F.; Zarkesh, R. A.; Heyduk, A. F. *Dalton Trans.* **2013**, *42*, 3751–3766.
- (12) Khusniyarov, M. M.; Weyhermueller, T.; Bill, E.; Wieghardt, K. *J. Am. Chem. Soc.* **2009**, *131*, 1208–1221.
- (13) Khusniyarov, M. M.; Bill, E.; Weyhermueller, T.; Bothe, E.; Harms, K.; Sundermeyer, J.; Wieghardt, K. *Chem.—Eur. J.* **2008**, *14*, 7608–7622.
- (14) Bill, E.; Bothe, E.; Chaudhuri, P.; Chlopek, K.; Herebian, D.; Kokatam, S.; Ray, K.; Weyhermueller, T.; Neese, F.; Wieghardt, K. *Chem.—Eur. J.* **2005**, *11*, 204–224.
- (15) Herebian, D.; Bothe, E.; Neese, F.; Weyhermueller, T.; Wieghardt, K. *J. Am. Chem. Soc.* **2003**, *125*, 9116–9128.
- (16) Chlopek, K.; Bill, E.; Ueller, T. W.; Wieghardt, K. *Inorg. Chem.* **2005**, *44*, 7087–7098.
- (17) Gorelsky, S. I.; Lever, A. B. P.; Ebadi, M. *Coord. Chem. Rev.* **2002**, *230*, 97–105.
- (18) Rajput, A.; Sharma, A. K.; Barman, S. K.; Koley, D.; Steinert, M.; Mukherjee, R. *Inorg. Chem.* **2014**, *53*, 36–48.
- (19) Chirik, P. J. *Inorg. Chem.* **2011**, *50*, 9737–9740.
- (20) Verma, P.; Weir, J.; Mirica, L.; Stack, T. D. P. *Inorg. Chem.* **2011**, *50*, 9816–9825.
- (21) Ray, K.; Petrenko, T.; Wieghardt, K.; Neese, F. *Dalton Trans.* **2007**, 1552–1566.
- (22) Chlopek, K.; Muresan, N.; Neese, F.; Wieghardt, K. *Chem.—Eur. J.* **2007**, *13*, 8390–8403.
- (23) Chaudhuri, P.; Verani, C. N.; Bill, E.; Bothe, E.; Weyhermueller, T.; Wieghardt, K. *J. Am. Chem. Soc.* **2001**, *123*, 2213–2223.
- (24) Weinberg, D. R.; Gagliardi, C. J.; Hull, J. F.; Murphy, C. F.; Kent, C. A.; Westlake, B. C.; Paul, A.; Ess, D. H.; McCafferty, D. G.; Meyer, T. J. *Chem. Rev.* **2012**, *112*, 4016–4093.
- (25) Huynh, M. H. V.; Meyer, T. J. *Chem. Rev.* **2007**, *107*, 5004–5064.
- (26) DuBois, D. L.; Bullock, R. M. *Eur. J. Inorg. Chem.* **2011**, 1017–1027.
- (27) Roubelakis, M. M.; Bediako, D. K.; Dogutan, D. K.; Nocera, D. G. *Energy Environ. Sci.* **2012**, *5*, 7737–7740.
- (28) Hoffman, B. M.; Lukoyanov, D.; Dean, D. R.; Seefeldt, L. C. *Acc. Chem. Res.* **2013**, *46*, 587–595.

- (29) Hoffman, B. M.; Dean, D. R.; Seefeldt, L. C. *Acc. Chem. Res.* **2009**, *42*, 609–619.
- (30) Matsumoto, T.; Chang, H.-C.; Wakizaka, M.; Ueno, S.; Kobayashi, A.; Nakayama, A.; Taketsugu, T.; Kato, M. *J. Am. Chem. Soc.* **2013**, *135*, 8646–8654.
- (31) Lu, F.; Zarkesh, R. A.; Heyduk, A. F. *Eur. J. Inorg. Chem.* **2012**, *2012*, 467–470.
- (32) Vaillancourt, F. H.; Bolin, J. T.; Eltis, L. D. *Crit. Rev. Biochem. Mol. Biol.* **2006**, *41*, 241–267.
- (33) Costas, M.; Mehn, M. P.; Jensen, M. P.; Que, L. *Chem. Rev.* **2004**, *104*, 939–986.
- (34) Lipscomb, J. D. *Curr. Opin. Struct. Biol.* **2008**, *18*, 644–649.
- (35) Emerson, J. P.; Kovaleva, E. G.; Farquhar, E. R.; Lipscomb, J. D.; Que, L. *Proc. Natl. Acad. Sci. U.S.A.* **2008**, *105*, 7347–7352.
- (36) Bittner, M. M.; Lindeman, S. V.; Fiedler, A. T. *J. Am. Chem. Soc.* **2012**, *134*, 5460–5463.
- (37) Bittner, M. M.; Kraus, D.; Lindeman, S. V.; Popescu, C. V.; Fiedler, A. T. *Chem.—Eur. J.* **2013**, *19*, 9686–9698.
- (38) Bittner, M. M.; Baus, J. S.; Lindeman, S. V.; Fiedler, A. T. *Eur. J. Inorg. Chem.* **2012**, 1848–1856.
- (39) Khomenko, T. M.; Salomatina, O. V.; Kurbakova, S. Y.; Il'ina, I. V.; Volcho, K. P.; Komarova, N. I.; Korchagina, D. V.; Salakhutdinov, N. F.; Tolstikov, A. G. *Russ. J. Org. Chem.* **2006**, *42*, 1653–1661.
- (40) Manner, V. W.; Markle, T. F.; Freudenthal, J. H.; Roth, J. P.; Mayer, J. M. *Chem. Commun.* **2008**, 256–258.
- (41) Stoll, S.; Schweiger, A. *J. Magn. Reson.* **2006**, *178*, 42–55.
- (42) Michaud-Soret, I.; Andersson, K. K.; Que, L., Jr.; Haavik, J. *Biochemistry* **1995**, *34*, 5504–10.
- (43) Sheldrick, G. M. *Acta Crystallogr., Sect. A* **2008**, *64*, 112–122.
- (44) Dolomanov, O. V.; Bourhis, L. J.; Gildea, R. J.; Howard, J. A. K.; Puschmann, H. *J. Appl. Crystallogr.* **2009**, *42*, 339–341.
- (45) Frantz, D. K.; Linden, A.; Baldrige, K. K.; Siegel, J. S. *J. Am. Chem. Soc.* **2012**, *134*, 1528–1535.
- (46) Kryatov, S. V.; Rybak-Akimova, E. V.; Schindler, S. *Chem. Rev.* **2005**, *105*, 2175–2226.
- (47) Battino, R.; Cleve, H. L. *Chem. Rev.* **1966**, *66*, 395–463.
- (48) Halder, P.; Paria, S.; Paine, T. K. *Chem.—Eur. J.* **2012**, *18*, 11778–11787, S11778/1–S11778/10.
- (49) Bruijninx, P. C. A.; Lutz, M.; Spek, A. L.; Hagen, W. R.; Weckhuysen, B. M.; van Koten, G.; Gebbink, R. J. M. *J. Am. Chem. Soc.* **2007**, *129*, 2275–2286.
- (50) Lin, G.; Reid, G.; Bugg, T. D. H. *J. Am. Chem. Soc.* **2001**, *123*, 5030–5039.
- (51) Jo, D.-H.; Chiou, Y.-M.; Que, L., Jr. *Inorg. Chem.* **2001**, *40*, 3181–3190.
- (52) Shaikh, N.; Panja, A.; Banerjee, P.; Ali, M. *Transition Met. Chem. (Dordrecht, Neth.)* **2003**, *28*, 871–880.
- (53) Neese, F. ORCA - An Ab Initio, DFT and Semiempirical Electronic Structure Package, version 2.9; Max Planck Institute for Bioinorganic Chemistry: Muelheim, Germany, 2012.
- (54) Becke, A. D. *J. Chem. Phys.* **1993**, *98*, 5648–5652.
- (55) Lee, C. T.; Yang, W. T.; Parr, R. G. *Phys. Rev. B* **1988**, *37*, 785–789.
- (56) Schafer, A.; Huber, C.; Ahlrichs, R. *J. Chem. Phys.* **1994**, *100*, 5829–5835.
- (57) Schafer, A.; Horn, H.; Ahlrichs, R. *J. Chem. Phys.* **1992**, *97*, 2571–2577.
- (58) Weigend, F.; Ahlrichs, R. *Phys. Chem. Chem. Phys.* **2005**, *7*, 3297–3305.
- (59) Stratmann, R. E.; Scuseria, G. E.; Frisch, M. J. *J. Chem. Phys.* **1998**, *109*, 8218–8224.
- (60) Casida, M. E.; Jamorski, C.; Casida, K. C.; Salahub, D. R. *J. Chem. Phys.* **1998**, *108*, 4439–4449.
- (61) Bauernschmitt, R.; Ahlrichs, R. *Chem. Phys. Lett.* **1996**, *256*, 454–464.
- (62) Hirata, S.; Head-Gordon, M. *Chem. Phys. Lett.* **1999**, *314*, 291–299.
- (63) Hirata, S.; Head-Gordon, M. *Chem. Phys. Lett.* **1999**, *302*, 375–382.
- (64) Laaksonen, L. *J. Mol. Graphics* **1992**, *10*, 33–&.
- (65) Perdew, J. P.; Burke, K.; Ernzerhof, M. *Phys. Rev. Lett.* **1996**, *77*, 3865–3868.
- (66) Klamt, A.; Schueuermann, G. *J. Chem. Soc., Perkin Trans. 2* **1993**, 799–805.
- (67) Despite repeated efforts, it was not possible to generate an Fe(II) complex containing the monoanionic form of ^{tbu}PDA, reflecting the weaker acidity of aryl amines relative to phenols and catechols.
- (68) The yellow color of [3]OTf is due to an absorption band near 400 nm that arises from a catecholate-to-iron(II) charge transfer (CT) transition. In the case of [4](OTf)₂, the ligand-based orbitals of neutral ^{tbu}PDA are stabilized relative to those of anionic ^{tbu}CatH. Thus, the corresponding ^{tbu}PDA-to-Fe(II) CT transition is shifted to higher energy and exists entirely in the UV region, resulting in a colorless complex.
- (69) Addison, A. W.; Rao, T. N.; Reedijk, J.; Vanrijn, J.; Verschoor, G. C. *J. Chem. Soc., Dalton Trans.* **1984**, 1349–1356.
- (70) Reynolds, M. F.; Costas, M.; Ito, M.; Jo, D.-H.; Tipton, A. A.; Whiting, A. K.; Que, L., Jr. *J. Biol. Inorg. Chem.* **2003**, *8*, 263–272.
- (71) Paria, S.; Halder, P.; Chakraborty, B.; Paine, T. K. *Indian J. Chem., Sect. A* **2011**, *50A*, 420–426.
- (72) Chiou, Y.-M.; Que, L., Jr. *Inorg. Chem.* **1995**, *34*, 3577–3578.
- (73) Park, H.; Baus, J. S.; Lindeman, S. V.; Fiedler, A. T. *Inorg. Chem.* **2011**, *50*, 11978–11989.
- (74) Baum, A. E.; Park, H.; Wang, D. N.; Lindeman, S. V.; Fiedler, A. T. *Dalton Trans.* **2012**, *41*, 12244–12253.
- (75) Masui, H.; Lever, A. B. P.; Auburn, P. R. *Inorg. Chem.* **1991**, *30*, 2402–10.
- (76) Comba, P.; Wadepohl, H.; Wunderlich, S. *Eur. J. Inorg. Chem.* **2011**, *2011*, 5242–5249.
- (77) Ogihara, T.; Hikichi, S.; Akita, M.; Moro-oka, Y. *Inorg. Chem.* **1998**, *37*, 2614–2615.
- (78) Jo, D.-H.; Que, L., Jr. *Angew. Chem., Int. Ed.* **2000**, *39*, 4284–4287.
- (79) Since MeCN was not used in the preparation of the MB samples, the minor species is not the six-coordinate structure obtained by XRD.
- (80) Peng, S. M.; Chen, C. T.; Liaw, D. S.; Chen, C. I.; Wang, Y. *Inorg. Chim. Acta* **1985**, *101*, L31–L33.
- (81) Bugarcic, T.; Habtemariam, A.; Deeth, R. J.; Fabbiani, F. P. A.; Parsons, S.; Sadler, P. J. *Inorg. Chem.* **2009**, *48*, 9444–9453.
- (82) Juestel, T.; Bendix, J.; Metzler-Nolte, N.; Weyhermueller, T.; Nuber, B.; Wieghardt, K. *Inorg. Chem.* **1998**, *37*, 35–43.
- (83) Venegas-Yazigi, D.; Mirza, H.; Lever, A. B. P.; Lough, A. J.; Costamagna, J.; Latorre, R. *Acta Crystallogr., Sect. C: Cryst. Struct. Commun.* **2000**, *C56*, e281–e282.
- (84) Holt, B. T. O.; Vance, M. A.; Mirica, L. M.; Heppner, D. E.; Stack, T. D. P.; Solomon, E. I. *J. Am. Chem. Soc.* **2009**, *131*, 6421–6438.
- (85) Hartl, F.; Stufkens, D. J.; Vlcek, A. *Inorg. Chem.* **1992**, *31*, 1687–1695.
- (86) Kapovsky, M.; Dares, C.; Dodsworth, E. S.; Begum, R. A.; Raco, V.; Lever, A. B. P. *Inorg. Chem.* **2013**, *52*, 169–181.
- (87) Fukuzumi, S.; Kotani, H.; Prokop, K. A.; Goldberg, D. P. *J. Am. Chem. Soc.* **2011**, *133*, 1859–1869.
- (88) Fukuzumi, S.; Kotani, H.; Lee, Y.-M.; Nam, W. *J. Am. Chem. Soc.* **2008**, *130*, 15134–15142.
- (89) Because of its fast nature, it was not possible to measure accurate activation parameters for the reaction of [3]⁺ with O₂ using conventional methods.
- (90) Warren, J. J.; Tronic, T. A.; Mayer, J. M. *Chem. Rev.* **2010**, *110*, 6961–7001.
- (91) Bordwell, F. G.; Cheng, J. P.; Harrelson, J. A. *J. Am. Chem. Soc.* **1988**, *110*, 1229–1231.
- (92) Bordwell, F. G.; Cheng, J. P. *J. Am. Chem. Soc.* **1991**, *113*, 1736–1743.
- (93) Bordwell, F. G.; Zhang, X. M.; Cheng, J. P. *J. Org. Chem.* **1993**, *58*, 6410–16.

- (94) Schenk, G.; Pau, M. Y. M.; Solomon, E. I. *J. Am. Chem. Soc.* **2004**, *126*, 505–515.
- (95) Diebold, A. R.; Straganz, G. D.; Solomon, E. I. *J. Am. Chem. Soc.* **2011**, *133*, 15979–15991.
- (96) Davis, M. I.; Wasinger, E. C.; Decker, A.; Pau, M. Y. M.; Vaillancourt, F. H.; Bolin, J. T.; Eltis, L. D.; Hedman, B.; Hodgson, K. O.; Solomon, E. I. *J. Am. Chem. Soc.* **2003**, *125*, 11214–11227.
- (97) Georgiev, V.; Borowski, T.; Blomberg, M. R. A.; Siegbahn, P. E. M. *J. Biol. Inorg. Chem.* **2008**, *13*, 929–940.
- (98) Christian, G. J.; Ye, S. F.; Neese, F. *Chem. Sci.* **2012**, *3*, 1600–1611.
- (99) Cramer, C. J.; Tolman, W. B.; Theopold, K. H.; Rheingold, A. L. *Proc. Natl. Acad. Sci. U.S.A.* **2003**, *100*, 3635–3640.
- (100) Chakraborty, B.; Paine, T. K. *Angew. Chem., Int. Ed.* **2013**, *52*, 920–924.
- (101) Mbughuni, M. M.; Chakrabarti, M.; Hayden, J. A.; Bominaar, E. L.; Hendrich, M. P.; Munck, E.; Lipscomb, J. D. *Proc. Natl. Acad. Sci. U.S.A.* **2010**, *107*, 16788–16793.
- (102) Mbughuni, M. M.; Chakrabarti, M.; Hayden, J. A.; Meier, K. K.; Dalluge, J. J.; Hendrich, M. P.; Munck, E.; Lipscomb, J. D. *Biochemistry* **2011**, *50*, 10262–10274.